Monthly Notices of the ROYAL ASTRONOMICAL SOCIETY

MNRAS **496,** 1307–1324 (2020) doi:10.1093/mnras/staa1538
Advance Access publication 2020 June 3

Testing the reliability of fast methods for weak lensing simulations: WL-MOKA on PINOCCHIO

Carlo Giocoli [1,2,3,4★] Pierluigi Monaco,[5,6,7,8] Lauro Moscardini,[1,3,4] Tiago Castro,[5,6,7,8] Massimo Meneghetti [3,4] R. Benton Metcalf[1,2] and Marco Baldi [1,3,4]

[1]*Dipartimento di Fisica e Astronomia, Alma Mater Studiorum Università di Bologna, via Gobetti 93/2, I-40129 Bologna, Italy*
[2]*Dipartimento di Fisica e Scienza della Terra, Università degli Studi di Ferrara, via Saragat 1, I-44122 Ferrara, Italy*
[3]*INAF – Astrophysics and Space Science Observatory Bologna, via Gobetti 93/3, I-40129 Bologna, Italy*
[4]*INFN – Sezione di Bologna, viale Berti Pichat 6/2, I-40127 Bologna, Italy*
[5]*Dipartimento di Fisica, Sezione di Astronomia, Università di Trieste, Via Tiepolo 11, I-34143 Trieste, Italy*
[6]*INAF – Osservatorio Astronomico di Trieste, via Tiepolo 11, I-34131 Trieste, Italy*
[7]*IFPU – Institute for Fundamental Physics of the Universe, via Beirut 2, I-34151 Trieste, Italy*
[8]*INFN – Sezione di Trieste, I-34100 Trieste, Italy*

Accepted 2020 May 28. Received 2020 May 24; in original form 2020 January 30

ABSTRACT

The generation of simulated convergence maps is of key importance in fully exploiting weak lensing by large-scale structure (LSS) from which cosmological parameters can be derived. In this paper, we present an extension of the PINOCCHIO code that produces catalogues of dark matter haloes so that it is capable of simulating weak lensing by Modify LSS into Large Scale Structures (LSS). Like WL-MOKA, the method starts with a random realization of cosmological initial conditions, creates a halo catalogue and projects it on to the past light-cone, and paints in haloes assuming parametric models for the mass density distribution within them. Large-scale modes that are not accounted for by the haloes are constructed using linear theory. We discuss the systematic errors affecting the convergence power spectra when Lagrangian perturbation theory at increasing order is used to displace the haloes within PINOCCHIO, and how they depend on the grid resolution. Our approximate method is shown to be very fast when compared to full ray-tracing simulations from an *N*-body run and able to recover the weak lensing signal, at different redshifts, with a few percent accuracy. It also allows for quickly constructing weak lensing covariance matrices, complementing PINOCCHIO's ability of generating the cluster mass function and galaxy clustering covariances and thus paving the way for calculating cross-covariances between the different probes. This work advances these approximate methods as tools for simulating and analysing survey data for cosmological purposes.

Key words: gravitational lensing: weak – galaxies: haloes – cosmology: theory – dark matter.

1 INTRODUCTION

Recent observational campaigns dedicated to the study of the distribution of matter on large scales such as the ones coming from the cosmic microwave background (CMB) fluctuations (Bennett et al. 2013; Planck Collaboration I 2014; Planck Collaboration XIII 2016), cosmic shear (Erben et al. 2013; Kilbinger et al. 2013; Hildebrandt et al. 2017), and galaxy clustering (Cole et al. 2005; Eisenstein et al. 2005; Sánchez et al. 2014) tend to favour the so-called standard cosmological model, where the energy–density of our Universe is dominated by two unknown forms: dark matter and dark energy (Peebles 1980, 1993). This model successfully predicts different aspects of structure formation processes (White & Rees 1978; Baugh 2006; Somerville & Davé 2015) going from the clustering of galaxies on very large scales (Zehavi et al. 2011; Marulli et al. 2013; Beutler et al. 2014) to galaxy clusters (Meneghetti et al. 2008; Postman et al. 2012; Meneghetti et al. 2014; Merten et al. 2015; Bergamini et al. 2019), to the properties of dwarf galaxies (Wilkinson et al. 2004; Madau, Diemand & Kuhlen 2008; Sawala et al. 2015; Wetzel et al. 2016).

Several experiments have been designed to constrain the cosmological parameters with percent accuracy, however some of them have revealed unexpected inconsistencies (Planck Collaboration

★ E-mail: carlo.giocoli@inaf.it

XXIV 2016). In particular, while the CMB temperature fluctuations probe the high-redshift Universe, gravitational lensing by large-scale structures (LSS) and cluster counts are sensitive to low-redshift density fluctuations. Recent comparisons between high- and low-redshift probes have shown some differences in the measured amplitude of the density fluctuations expressed through the parameter σ_8: CMB power spectrum from Planck prefers a slightly higher value of σ_8 with respect to the ones coming from cosmic shear and cluster counts.

Gravitational lensing is a fundamental tool to study and map the matter density distribution in our Universe (Bartelmann & Schneider 2001; Kilbinger 2015). For instance, while galaxy clustering measurements probe the matter density field subject to the galaxy bias (Sánchez et al. 2012; Marulli et al. 2013; Percival et al. 2014; Sánchez et al. 2014; Lee et al. 2019), tomographic lensing analyses open the possibility of reconstructing the projected total matter density distribution as a function of redshift, and thus trace the cosmic structure formation in time (Benjamin et al. 2013; Kitching et al. 2014; Hildebrandt et al. 2017; Kitching et al. 2019). Since lensing is sensitive to the total matter density present between the source and the observer, it does not rely on any assumptions about the correlation between luminous and dark matter. It is also very sensitive to the presence of massive neutrinos as they tend to suppress the growth of density fluctuations (Lesgourgues & Pastor 2006; Castorina et al. 2014; Massara, Villaescusa-Navarro & Viel 2014; Carbone, Petkova & Dolag 2016; Poulin et al. 2018), thus introducing a degeneracy with σ_8.

In order to better understand said inconsistency between low- and high-redshift probes – e.g. whether it comes from new physics or due to systematics in the data analyses – more dedicated measurements are needed to reduce the statistical error bars and possibly reveal a significant tension. For instance, weak gravitational lensing caused by LSS, usually dubbed cosmic shear, will represent one of the primary cosmological probes of various future wide-field surveys, like for example the ESA Euclid mission (Laureijs et al. 2011) and LSST (Ivezic et al. 2009; LSST Science Collaboration 2009). When the number of background sources, used to derive the lensing signal, is large, the reconstruction of cosmological parameters depends mainly on the control we have on systematics and covariances down to the typical scale that is probed by the weak gravitational lensing measurements. The construction of the covariance matrix requires the production of a large sample of realizations that are able to not only take into account all possible effects expected to be found in observations but also to mimic as closely as possible the actual survey.

In this work, we present an extension of the latest version of PINOCCHIO (Munari et al. 2017) that starts from the halo catalogue constructed within a past light-cone (hereafter PLC) and simulates the weak lensing signal generated by the intervening matter density distribution up to a given source redshift. We have interfaced the PLC output with WL-MOKA (Giocoli et al. 2017) in order to construct the convergence map due to the intervening haloes. These algorithms together reduce the computational cost of simulating the PLC on cosmological scales by more than one order of magnitude with respect to other methods based on *N*-body simulations, allowing the construction of a very large sample of simulated weak lensing PLCs to derive covariance matrices and, in a future work, also to inspect the cosmological dependence of covariances.

The paper is organized as follows. In Section 2, we introduce our method presenting the simulation data set. In Section 3, we present our light-cone simulations and power spectrum measurements. We summarize and conclude in Section 4.

2 METHODS AND SIMULATIONS

In this section, we describe the reference cosmological numerical simulation with which we compare our approximate methods for weak gravitational lensing simulations, and present our algorithms.

2.1 Weak lensing maps from *N*-body simulations

In this work, we have used the lambda cold dark matter (ΛCDM) run of the CoDECS project (Baldi 2012) as our reference *N*-body simulation. The run has been performed using a modified version of the widely used TREEPM/SPH *N*-body code GADGET (Springel 2005) developed in Baldi et al. (2010).[1] The CoDECS simulations adopt the following cosmological parameters, consistent with the WMAP7 constraints by Komatsu et al. (2011): $\Omega_{\rm CDM} = 0.226$, $\Omega_{\rm b} = 0.0451$, $\Omega_\Lambda = 0.729$, $h = 0.703$, and $n_{\rm s} = 0.966$, with the initial amplitude of linear scalar perturbations at CMB time ($z_{\rm CMB} \approx 1100$) set to $\mathcal{A}_s(z_{\rm CMB}) = 2.42 \times 10^{-9}$, resulting in a value of $\sigma_8 = 0.809$ at $z = 0$.

The *N*-body run follows the evolution 2×1024^3 particles evolved through collisionless dynamics from $z = 99$ to $z = 0$ in a comoving box of 1 Gpc h^{-1} by side. The mass resolution is $m_{\rm CDM} = 5.84 \times 10^{10}$ $\mathrm{M}_\odot\, h^{-1}$ for the cold dark matter component and $m_{\rm b} = 1.17 \times 10^{10}$ $\mathrm{M}_\odot\, h^{-1}$ for baryons, while the gravitational softening was set to $\epsilon_{\rm g} = 20\,\mathrm{kpc}\, h^{-1}$. Despite the presence of baryonic particles, this simulation does not include hydrodynamics and is therefore a purely collisionless *N*-body run. This is due to the original purpose of the CoDECS simulations to capture the non-universal coupling of a light dark energy scalar field to dark matter particles only, leaving baryons uncoupled. Clearly, for the reference ΛCDM run – where the coupling is set to zero – no difference is to be expected in the gravitational evolution of the dark matter and baryonic components, which should be considered just as two families of collisionless particles.

To build the lensing maps for light-cone simulations, we stacked together different slices of the simulation snapshots up to $z_{\rm s} = 4$. We have constructed the PLC to have an angular squared aperture of 5 deg on a side, which combined with the comoving size of the simulation box of 1 Gpc h^{-1}, ensures that the mass density distribution in the cone has no gaps. By construction, the geometry of the PLC is a pyramid with a squared base, where the observer is located at the vertex of the solid figure, while the final source redshift is placed at the base. In stacking up the various simulation snapshots and collapsing them into projected particle lens planes, we make use of the MAPSIM code (Giocoli et al. 2015; Tessore et al. 2015; Castro et al. 2018; Hilbert et al. 2020). The code initializes the memory and the grid size of the maps and reads particle positions within the desired field of view (in this case, 5 deg on a side) from single snapshot files, which reduces the memory consumption significantly. The algorithm builds up the lens planes from the present time up to the highest source redshift, selected to be $z_{\rm s} = 4$. The number of required lens planes is decided ahead of time in order to avoid gaps in the constructed light-cones. The lens planes are built by mapping the particle positions to the nearest predetermined plane, maintaining angular positions, and then pixelizing the surface density using the triangular shaped cloud (TSC) mass assignment

[1] In Baldi et al. (2010), GADGET has been extended to cosmological scenarios with non-minimal couplings between dark energy and cold dark matter particles. In this work, we are limiting our analysis to the standard vanilla-ΛCDM cosmology, thereby employing only the reference ΛCDM run of the CoDECS simulations suite.

scheme (Hockney & Eastwood 1988). The grid pixels are chosen to have the same angular size on all planes, equal to 2048×2048, which allows for a resolution of 8.8 arcsec per pixel. The lens planes have been constructed each time a piece of simulation is taken from the stored particle snapshots; their number and recurrence depend on the number of snapshots stored while running the simulation. In particular, in running our simulation we have stored 17 snapshots from $z \sim 4$ to $z = 0$. In Castro et al. (2018), it has been shown that a similar number of snapshots are enough to reconstruct the PLC up to $z \sim 5$ with lensing statistics changing by less than 1 per cent if more snapshots are used.

The selection and the randomization of each snapshot is done as in Roncarelli et al. (2007) and discussed in more detail in Giocoli et al. (2015). If the light-cone arrives at the border of a simulation box before it reaches the redshift limit where the next snapshot will be used, the box is re-randomized and the light-cone extended through it again. Once the lens planes are created, the lensing calculation itself is done using the ray-tracing GLAMER pipeline (Metcalf & Petkova 2014; Petkova, Metcalf & Giocoli 2014). In order to have various statistical samples, we have created 25 light-cone realizations. They can be treated as independent since they do not contain the same structures along the line of sight, considering the size of the simulation box to be 1 Gpc h^{-1} and the field of view of 5 deg on a side. However, it is worth mentioning that all the light-cones are constructed from the same *N*-body run and that they share the same random realization of the initial conditions (ICs) of the Universe. Even if their reconstructed lensing signal on small scales depends on matter that occurs in the field of view, the large-scale modes are established by the seed in the ICs set-up when running the numerical simulation.

2.2 Approximate past light-cones using PINOCCHIO

We will compare the lensing simulations performed using the *N*-body run, with the ones constructed from the halo catalogues built up using a fast and approximate algorithm: PINOCCHIO (namely its version 4.1.1).

PINOCCHIO is an approximate, semi-analytic public code,[2] based on excursion-set theory, ellipsoidal collapse, and Lagrangian perturbation theory (LPT), that is able to predict the formation of dark matter haloes, given a cosmological linear density field generated on a grid, without running a full *N*-body simulation. It was presented in Monaco, Theuns & Taffoni (2002), then extended in Monaco et al. (2013) and Munari et al. (2017). The code first generates a density contrast field on a grid, then it Gaussian-smooths the density using several smoothing radii and computes, using ellipsoidal collapse, the collapse time at each grid point (particle), storing the earliest value. Later, it fragments the collapsed medium with an algorithm that mimics the hierarchical formation of structure. Dark matter haloes are displaced to their final position using LPT. The user can choose which perturbation order to adopt: Zel'dovich approximation (ZA), second-order (2LPT), or third-order (3LPT).

Outputs are given both at fixed times and on the light-cone (Munari et al. 2017): for each halo, and for a list of periodic replications needed to tile the comoving volume of the light-cone, the code computes the time at which the object crosses the light-cone, and outputs its properties (mass, position, and velocity) at that time.

Using PINOCCHIO, we have produced different simulations as summarized in Table 1. We set cosmology and box properties identical to those used for the reference *N*-body simulation, but with different initial seed numbers so as to have several realizations of the same volume. This allows us to beat down sample variance on the predicted convergence power spectrum. Our reference PINOCCHIO simulation has been run with 1024^3 grid points and in the 3LPT configuration for the particle displacements starting from the ICs. This run consists of 512 different realizations and corresponding PLCs. We have chosen the semi-aperture of the PLC to be 7.1 deg which gives a total area in the plane of the sky of 158.37 deg^2. This value guarantees us the possibility of creating a pyramidal configuration for the convergence maps – consistent with the maps constructed from the *N*-body simulation – with 5 deg by side up to a final source redshift $z_s = 4$. In addition to the reference PINOCCHIO$_{3LPT}$, we produced a sample of other approximate simulations: 25 using the same grid resolutions but adopting both 2LPT and ZA displacements, 512 with a lower resolution grid (512^3) and 3LPT, and 25 with a higher resolution grid (2048^3) and 3LPT displacements. All corresponding mass resolutions are reported in the third column of Table 1. The random numbers of the ICs for the various PINOCCHIO simulations have been consistently chosen to be identical, in the sense that the 512 low-resolution runs with 512^3 grid size have the same initial random displacement fields of the 1024^3, and so the 25 runs performed with the different displacement fields or using a higher resolution grid of 2048^3 that share the IC seeds with the first 25 reference runs. This will allow us a more direct comparison between the different runs and convergence maps starting from the same initial displacement field of the theoretical linear power spectrum.

The typical CPU for a 1024^3 in 1 Gpc h^{-1} *N*-body simulations from $z = 99$ to $z = 0$, plus i/o 90 snapshots, and on-the-fly halo finding procedures is approximately 50 000 CPU hours; plus 1000 more hours for light-cone productions and multiplane ray tracing, a typical super architecture like the ones available at CINECA.[3] As for the required resources, a PINOCCHIO run with 1024^3 particles demands a CPU time of order of 10 h on a supercomputer; the version with Zel'dovich or 2LPT displacements can fit into a single node with 256 Gb of RAM, while the 3LPT version will require more memory; the elapsed time will be of order of 10 min in this case. Higher orders require a few more FFTs, for an overhead of order of $\sim$10 per cent going from Zel'dovich to 3LPT. The light-cone on-the-fly construction requires an even smaller overhead, $\sim$4 per cent for the configuration used in this paper. The scaling was demonstrated in Munari et al. (2017) to be very similar to $N\log_2 N$, so going from 512^3 to 1024^3, or from this to 2048^3, requires a factor of $\sim$9 more computing time and a factor of 8 more memory; if the number of used cores increases as the RAM, the wall-clock time will not change much. Painting haloes on the PLC halo catalogues takes not more than 2 CPU hours per light-cone, scaling with the number density of systems that depends on the minimum mass threshold considered and on maximum source redshift. This means a ratio of CPU times between full *N*-body and fast approximate methods in producing one convergence map of 5 deg by side of approximately 3×10^3. To these, we have to highlight the fact that each PINOCCHIO light-cone has the advantage of having a different IC set-up, while this is not the case for PLCs extracted from the *N*-body.

In the left-hand panel of Fig. 1, we show the comoving halo distribution in the PLCs constructed by PINOCCHIO; haloes have

[2] https://github.com/pigimonaco/Pinocchio

[3] http://www.hpc.cineca.it/content/hardware

Table 1. Summary of the simulations. The symbol $*$ marks our reference PINOCCHIO run. For the *N*-body case, it is worth mentioning that all the various light-cones have been generated from the same cosmological simulation, randomizing the various snapshots using the MAPSIM code. By construction, the particle mass resolution of our reference PINOCCHIO run is equal to that of the *N*-body simulation; all the runs consider a cosmological box of 1 Gpc h^{-1} comoving by side.

	Field of view [deg^2] (haloes)	Min. halo mass [M$_\odot/h$]	N. real.	Field of view [deg^2] (convergence)
($*$) PINOCCHIO$_{3LPC}$ (1024^3)	158.37	7.0×10^{11}	512	25
PINOCCHIO$_{2LPC}$ (1024^3)	158.37	7.0×10^{11}	25	25
PINOCCHIO$_{ZA}$ (1024^3)	158.37	7.0×10^{11}	25	25
PINOCCHIO$_{3LPC}$ (512^3)	158.37	5.6×10^{12}	512	25
PINOCCHIO$_{3LPC}$ (2048^3)	158.37	8.75×10^{10}	25	25
N-body	100	7.0×10^{10} (total part. mass: DM + bar.)	25	25

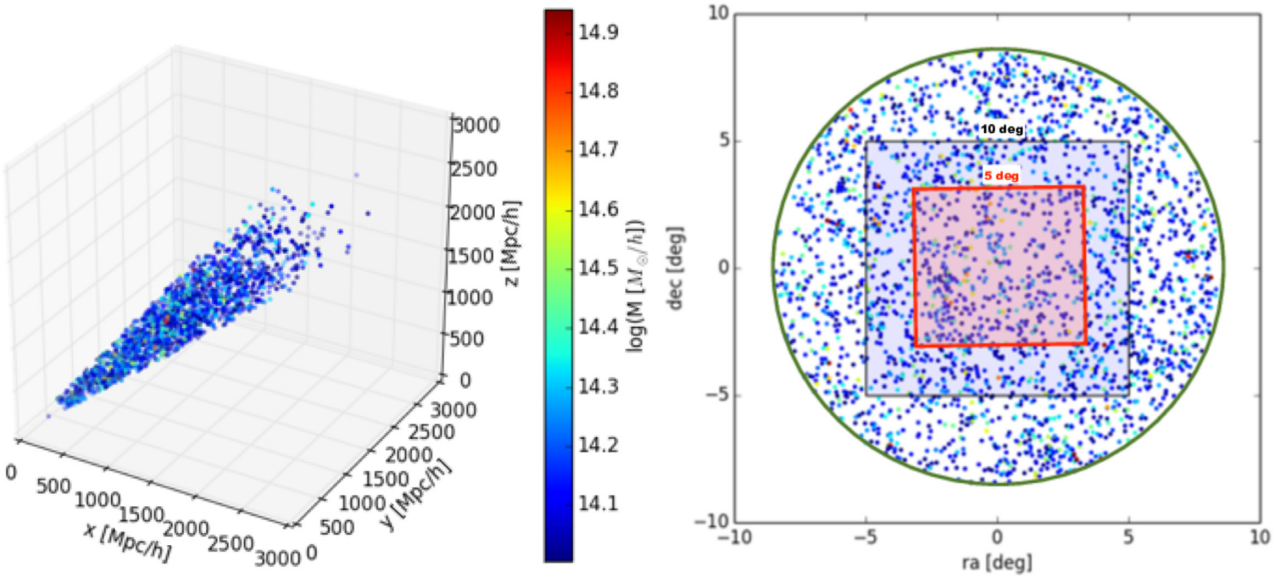

Figure 1. Geometrical construction of the comoving PLC in PINOCCHIO. In the left-hand panel, we show the comoving distribution of haloes with mass larger than 10^{14} M$_\odot$ h^{-1} up to redshift $z = 4$ present within one realization. The different masses are colour coded as indicated by the colour bar. In the right-hand panel, we display the two-dimensional distribution of those haloes on the plane of the sky in angular coordinates. In this case, the choice we have made about the angular geometry of the cone is more visible. The semi-aperture has been set to 7.1 deg which ensures that a square convergence map with 5 deg on a side can be simulated. This allows us to take into account the lensing contribution from haloes outside the field of view, from a buffer region, and reduce border effects.

different colour according to their mass, as indicated by the colour bar. In the right-hand panel, we display the two-dimensional distribution of haloes, in angular coordinates as they appear in the plane of the sky up to $z = 4$. In the right-hand panel, we draw also the size of the squared postage stamp of 5 deg by side representing the geometry of our final convergence map. The geometry of PINOCCHIO PLC allows us to consider the lensing contribution from haloes outside the field of view, from a buffer region, and accounting also for border effects: lensing signal due to haloes that are not in the final field of 5 deg by side.

In Fig. 2, we show the cumulative halo mass function normalized to a one square degree light-cone, from $z = 0$ up to redshift 0.5, 1.4, and 4 from bottom to top, respectively. In both cases, haloes have been identified using a Friends-of-Friends (FoF) algorithm. It is worth to underline that in PINOCCHIO the expression for the threshold distance that determines accretion and merging includes free parameters (Munari et al. 2017) as the linking length parameter for the FoF definition in the *N*-body simulations. The comparison of the FoF mass functions between PINOCCHIO and *N*-body simulation is fair and consistent, indeed in both cases we use the same methodology to find collapsed structures. For comparison, the dotted red curves display the FoF mass function as calibrated by Watson et al. (2013). The lower panels display the relative differences of the median counts computed averaging 25 different simulation light-cones of the *N*-body run with respect to the average predictions from the 512 PINOCCHIO simulations; the shaded area gives the sample variance measured with the quartiles from PINOCCHIO runs, that is large at low z due to the small sampled volume. Only for comparison purpose, in the top panel we show also the expectation from Sheth & Tormen (1999), where they use the virial definition for the halo mass, and from Tinker et al. (2008) and Despali et al. (2016) assuming a threshold corresponding to 200 times the comoving background density, which has been shown to be the closest to the FoF mass functions (Knebe et al. 2011). In the lower panel, we notice that there is a very good agreement between the halo counts in the *N*-body and PINOCCHIO light-cones down to 5×10^{12} M$_\odot$ h^{-1}, however, the higher the redshift the more the *N*-body counts suffer from a small reduction towards small masses due to particle and force resolutions. The error bars on the green data points and the grey shaded regions enclosing the black lines bracket the first and the third quartiles of the distribution at a fixed halo mass.

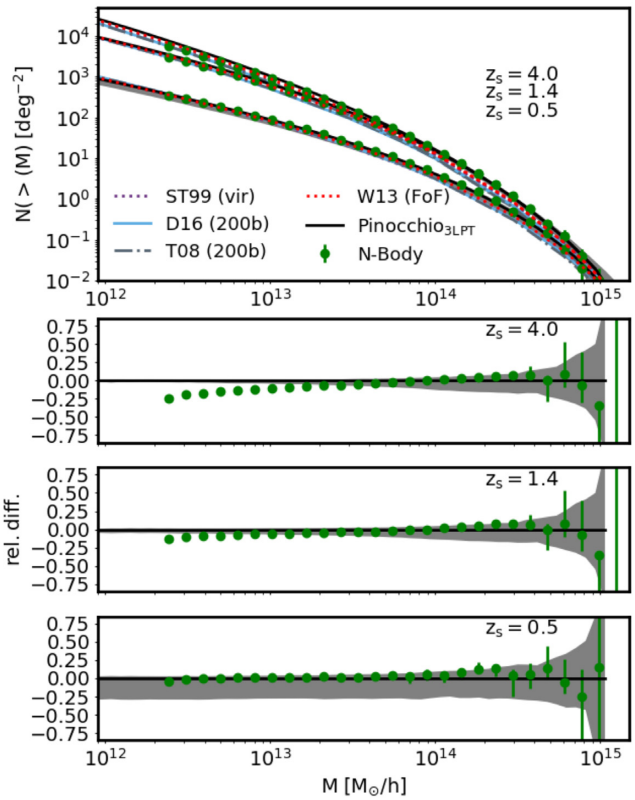

Figure 2. Cumulative halo mass function in unit of square degree within the constructed PLCs. The solid black curves display the median over the various realizations, the shaded grey area encloses the quartiles. The green data points indicate the median measurements from the *N*-body simulation over 25 different light-cones. The dotted magenta, solid light blue, dot–dashed dark grey, and red dotted display the predictions from Sheth & Tormen (1999), Despali et al. (2016), Tinker et al. (2008), and Watson et al. (2013) mass functions, respectively. The three bottom sub-panels show the relative difference between the mass function from the *N*-body and PINOCCHIO simulations, up to the three considered source redshifts.

2.2.1 *Weak lensing simulations using projected halo model*

In this section, we introduce the lensing notations we will adopt throughout the paper; the symbols and the equations are quite general and consistent between the two methods adopted in constructing the convergence maps from particles and haloes.

Defining $\boldsymbol{\theta}$ as the angular position on the sky and $\boldsymbol{\beta}$ as the position on the source plane (the unlensed position), then a distortion matrix $\mathbf{A}$, in the weak lensing regime, can be read as

$$\mathbf{A} \equiv \frac{\partial \boldsymbol{\beta}}{\partial \boldsymbol{\theta}} = \begin{pmatrix} 1-\kappa-\gamma_1 & \gamma_2 \\ \gamma_2 & 1-\kappa+\gamma_1 \end{pmatrix}, \tag{1}$$

where scalar κ represents the convergence and the pseudo-vector $\boldsymbol{\gamma} \equiv \gamma_1 + i\gamma_2$ the shear tensor.[4] In the case of a single lens plane, the convergence can be written as

$$\kappa(\boldsymbol{\theta}) \equiv \frac{\Sigma(\boldsymbol{\theta})}{\Sigma_{\rm crit}}, \tag{3}$$

where $\Sigma(\boldsymbol{\theta})$ represents the surface mass density and $\Sigma_{\rm crit}$ the critical surface density:

$$\Sigma_{\rm crit} \equiv \frac{c^2}{4\pi G}\frac{D_{\rm l}}{D_{\rm s} D_{\rm ls}}, \tag{4}$$

where c indicates the speed of light, G the Newton's constant, and $D_{\rm l}$, $D_{\rm s}$, and $D_{\rm ls}$ the angular diameter distances between observer lens, observer source, and source lens, respectively.

Following a general consensus, we will assume that matter in haloes is distributed following the Navarro, Frenk & White (1996, hereafter NFW) relation:

$$\rho(r|M_{\rm h}) = \frac{\rho_{\rm s}}{(r/r_{\rm s})(1+r/r_{\rm s})^2}, \tag{5}$$

where $r_{\rm s}$ is the scale radius, defining the concentration $c_{\rm h} \equiv R_{\rm h}/r_{\rm s}$ and $\rho_{\rm s}$ the dark matter density at the scale radius:

$$\rho_{\rm s} = \frac{M_{\rm h}}{4\pi r_{\rm s}^3}\left[\ln(1+c_{\rm h}) - \frac{c_{\rm h}}{1+c_{\rm h}}\right]^{-1}, \tag{6}$$

$R_{\rm h}$ is the radius of the halo which may vary depending on the halo overdensity definition.

From the hierarchical clustering model, the halo concentration $c_{\rm h}$ is expected to be a decreasing function of the host halo mass. Small haloes form first (van den Bosch 2002; De Boni et al. 2016) when the universe was denser and then merge together forming the more massive ones: galaxy clusters sit at the peak of the hierarchical pyramid being the most recent structures to form (Bond et al. 1991; Lacey & Cole 1993; Sheth & Tormen 2004a; Giocoli et al. 2007). This trend is reflected in the mass–concentration relation: at a given redshift smaller haloes are more concentrated than larger ones. Different fitting functions for mass–concentration relations have been presented by various authors (Bullock et al. 2001; Neto et al. 2007; Duffy et al. 2008; Gao et al. 2008; Meneghetti et al. 2014; Ragagnin et al. 2019). In this work, we adopt the relation proposed by Zhao et al. (2009) that links the concentration of a given halo with the time $t_{0.04}$ at which its main progenitor assembles 4 percent of its mass. For the mass accretion history, we adopt the model proposed by Giocoli, Tormen & Sheth (2012b) that allows us to trace back the full halo growth history with cosmic time down to the desired time $t_{0.04}$. We want to underline that the model by Zhao et al. (2009) also fits numerical simulations with different cosmologies; it seems to be of reasonably general validity within a few percent accuracy, as is the generalized model of the mass accretion history we adopt as tested by Giocoli et al. (2013). It is interesting to notice that the particular model for the concentration–mass relation mainly impacts on the behaviour of the power spectrum at scales below $1\,h^{-1}$Mpc as discussed in detail by Giocoli et al. (2010b). Due to different assembly histories, haloes with the same mass at the same redshift may have different concentrations (Navarro et al. 1996; Jing 2000; Wechsler et al. 2002; Zhao et al. 2003a,b). At fixed halo mass, the distribution in concentration is well described by a lognormal distribution function with an rms $\sigma_{\ln c}$ between 0.1 and 0.25 (Jing 2000; Dolag et al. 2004; Sheth & Tormen 2004b; Neto et al. 2007). In this work, we adopt a lognormal distribution with $\sigma_{\ln c} = 0.25$. We decided to follow this approach in assigning the halo concentration to be as general as possible. Results from the analyses of various numerical simulations have revealed that,

[4] In tensor notation we can read the shear as

$$\begin{pmatrix} \gamma_1 & \gamma_2 \\ \gamma_2 & -\gamma_1 \end{pmatrix}. \tag{2}$$

at fixed halo mass, structural properties, like concentration and subhalo population, depend on the halo assembly histories (Giocoli, Tormen & van den Bosch 2008; Giocoli et al. 2010a, 2012b; Lange et al. 2019; Zehavi et al. 2019; Chen et al. 2020; Montero-Dorta et al. 2020). However, saving all those data three files of the halo catalogues would have increased much the storage capability we planned for this project. As test case in Giocoli et al. (2017), we have also generated the halo convergence maps reading the halo concentration from the corresponding simulated *N*-body catalogue finding that the assembly bias effect on the convergence power spectra has only sub percent effects.

As presented by Bartelmann (1996), assuming spherical symmetry, the NFW profile has a well-defined solution when integrated along the line of sight up to the virial radius:

$$\kappa(x_1, x_2|M_{\rm h}, z_{\rm l}, z_{\rm s}) = 2\int_0^{R_{\rm vir}} \rho(x_1, x_2, \zeta|M_{\rm h}){\rm d}\zeta / \Sigma_{\rm crit}(z_{\rm l}, z_{\rm s}) \quad (7)$$

with $r^2 = x_1^2 + x_2^2 + \zeta^2$ (Giocoli et al. 2012a, 2017). Expressing $\xi^2 = x_1^2 + x_2^2$, we can write

$$\kappa_0 = 2.0/\Sigma_{\rm crit}(z_{\rm l}, z_{\rm s}), \quad (8)$$

and

$$\kappa(\xi) = \kappa_0(\kappa_1 + \kappa_2 + \kappa_3)/\kappa_D, \quad (9)$$

with

$$\begin{cases} \text{for } \xi < 1: \\ \kappa_1 = R_{\rm vir}\sqrt{1-\xi^2}\left(1 - \sqrt{\xi^2 + R_{\rm vir}^2}\right) \\ \kappa_2 = -\dfrac{\xi^2 + R_{\rm vir}^2 - 1}{2}\log\left(\dfrac{\frac{R_{\rm vir}}{\sqrt{1-\xi^2}} + 1}{\frac{R_{\rm vir}}{\sqrt{1-\xi^2}} - 1}\right) \\ \kappa_3 = \dfrac{\xi^2 + R_{\rm vir}^2 - 1}{2}\log\left(\dfrac{\left(\frac{R_{\rm vir}}{\sqrt{1-\xi^2}\sqrt{\xi^2 + R_{\rm vir}^2}}\right) + 1}{\left(\frac{R_{\rm vir}}{\sqrt{1-\xi^2}\sqrt{\xi^2 + R_{\rm vir}^2}}\right) - 1}\right) \\ \kappa_D = \left(1-\xi^2\right)^{3/2}\left(\xi^2 + R_{\rm vir}^2 - 1\right) \end{cases} \quad (10)$$

$$\begin{cases} \text{for } \xi > 1: \\ \kappa_1 = R_{\rm vir}\sqrt{\xi^2 - 1}\left(\sqrt{\xi^2 + R_{\rm vir}^2} - 1\right) \\ \kappa_2 = -\left(\xi^2 + R_{\rm vir}^2 - 1\right)\arctan\left(\dfrac{R_{\rm vir}}{\sqrt{\xi^2 - 1}}\right) \\ \kappa_3 = \left(\xi^2 + R_{\rm vir}^2 - 1\right)\arctan\left(\dfrac{R_{\rm vir}}{\sqrt{\xi^2 - 1}\sqrt{\xi^2 + R_{\rm vir}^2}}\right) \\ \kappa_D = \left(\xi^2 - 1\right)^{3/2}\left(\xi^2 + R_{\rm vir}^2 - 1\right) \end{cases} \quad (11)$$

and

$$\begin{cases} \text{for } \xi = 1: \\ \kappa(\xi) = \dfrac{\kappa_0}{3}\sqrt{1 + \dfrac{1}{R_{\rm vir}^2}}. \end{cases} \quad (12)$$

The contribution to the convergence from each halo within the field of view is modulated by the critical density that depends on the observer-lens-source configuration, as we have expressed in the equations above.

In the left-hand panel of Fig. 3, we show the convergence map reconstructed using halo positions, masses, and redshift from one PLC realization and assuming a fixed source redshift of $z_{\rm s} = 1.4$. We can see the contribution from all the mass in the haloes and the presence of galaxy clusters at the intersections of filaments. As discussed by Giocoli et al. (2017), the reconstructed power spectrum using only haloes fails in reproducing the expectation on large scales from linear theory. This inconsistency is a manifestation of the absence of large-scale modes sampled by small-mass haloes (below our mass resolution threshold) and by the diffuse matter that is not in haloes. A straightforward way to add this power back is to project on the PLC particle positions that are outside haloes, construct density planes in redshift bins, and add them to those obtained with haloes. This procedure is feasible and will be presented in a future paper; however, it implies significant overhead in CPU time and storage: it requires writing particle properties to the disc, something that is avoided by PINOCCHIO in its standard implementation. In the context of the massive generation of mock halo catalogues, it is very convenient to adopt the procedure proposed by Giocoli et al. (2017) to reconstruct the missing power from the halo catalogue itself. We have also estimated the effect of including in the models the missing diffuse matter present between haloes by extending the truncation of the density profile at different values of the virial radius. This effect mainly manifests in the transition between the 1- and 2-halo term up to large scales and has not much effect at the 1-halo level, in the projected power spectrum. The extension of the halo density profiles outside the virial radii creates a trend with the source redshifts, artificially increasing the mean background density of the universe, due to the projected intervening matter density distribution along the line of sight. None the less, we decided to be conservative in our method, as typically done in the halo model formalism (Cooray & Sheth 2002), assuming the collapsed matter in haloes only up to the virial radius.

In order to include the large scale modes due to unresolved matter not in haloes, we generate in Fourier space a field with a random Gaussian realization whose amplitude is modulated by $P_{\kappa,\rm lin}(l)$. The phases are chosen to be coherent with the halo location within the considered map (Giocoli et al. 2017). By construction, summing the convergence maps of the haloes with the one from the linear theory contribution gives a two-dimensional map that includes the cross-talk term between the two fields:

$$\begin{aligned} \langle\hat{\kappa}(\mathbf{l})\hat{\kappa}^*(\mathbf{l}')\rangle &= \langle(\widehat{\kappa_{\rm hm} + \kappa_{\rm lin}})(\mathbf{l})(\widehat{\kappa_{\rm hm} + \kappa_{\rm lin}})^*(\mathbf{l})\rangle \\ &= 4\pi^2\delta_D(\mathbf{l} - \mathbf{l}')\left(P_{\kappa_{\rm hm}}(l) + P_{\kappa_{\rm lin}}(l) + P_{\rm hm-lin}(l)\right), \end{aligned} \quad (13)$$

where $P_{\rm hm\text{-}lin}(l)$ indicates the cross-spectrum term between the two fields and, by definition, $P_{\kappa_{\rm lin}}(l) = P_{\kappa_{\rm lin,r}}(l)$, where $P_{\kappa_{\rm lin,r}}(l)$ indicates the power spectrum of a map with random phases. Because of the cross-spectrum term, we then re-normalize the map to match the large-scale behaviour predicted on large scale by linear theory using the relation:

$$A(l) = \frac{P_{\kappa,\rm lin}(l)}{P_{\kappa_{\rm hm}+\kappa_{\rm lin}}(l)}, \quad (14)$$

where $P_{\kappa_{\rm hm}+\kappa_{\rm lin}}(l) = P_{\kappa_{\rm hm}}(l) + P_{\kappa_{\rm lin}}(l) + P_{\rm hm-lin}(l)$.[5] Dividing the contributions to the convergence power spectrum in haloes and diffuse component allows us to discriminate two separate contributions. While the diffuse matter, relevant on large scales and

[5]We have also tested the case of subtracting the cross-talk spectra to the total power. However, it is worth mentioning that this gives the same results.

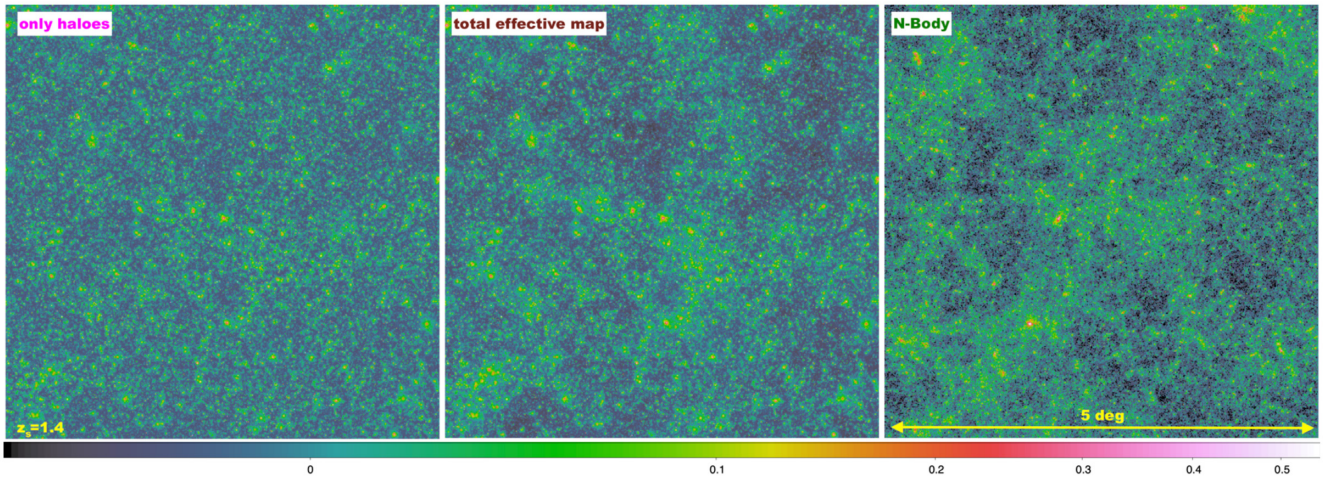

Figure 3. Convergence maps for sources at $z_s = 1.4$ for a field of view of 5×5 square degrees. Left-hand panel shows the map obtained from the halo catalogue of a PINOCCHIO PLC. Central panel displays the effective total contribution of haloes plus not resolved in haloes, modelled using linear theory. Right-hand panel shows, for comparison, the convergence map of a light-cone constructed using MAPSIM from the snapshots of a cosmological numerical simulation with a different realization of the ICs.

treated using linear theory, represents the Gaussian contribution to the power spectrum, the haloes, important on small scales in the non-linear regime, portrays the non-Gaussian stochastic part. Haloes are non-linear regions of the matter density fluctuation field disjoint from the expansion of the universe, their structural properties – concentration, substructures, density profiles, etc. – shape the small-scale modes (Cooray & Sheth 2002; Sheth & Jain 2003; Smith et al. 2003; Giocoli et al. 2010b).

In the central panel of Fig. 3, we display the convergence map where we include also the modelling of the large-scale modes coherent with the halo distribution within the field of view. In order to do so, we use as reference the prediction, in the Fourier space, from the linear theory of the convergence power spectrum $P_{\kappa,\rm lin}(l)$ that in the Born approximation and for source redshift at z_s can be read as

$$P_{\kappa,\rm lin}(l) = \frac{9H_0^4\Omega_{\rm m}^2}{4c^4}\int_0^{w_s(z_s)}\left(\frac{D(z,z_s)}{D(z_s)a}\right)^2 P_{\delta,\rm lin}\left(l\frac{a}{D(z)},z\right)\,{\rm d}w, \tag{15}$$

where H_0 and $\Omega_{\rm m}$ represent the present-day Hubble constant and matter density parameter, c indicates the speed of light, $w(z)$ and $D(z)$ the radial comoving and angular diameter distances at redshift z, $a \equiv 1/(1+z)$, and $P_{\delta,\rm lin}(k, z)$ the linear matter power spectrum at a given comoving mode k re-scaled by the growth factor at redshift z. For comparison, the third panel of Fig. 3 displays the convergence map of the PLC constructed from the cosmological numerical simulation up to $z_s = 1.4$; we recall that the simulation *does not* trace the same LSS as the PINOCCHIO realization.

2.3 Halo model for non-linear power spectrum

The non-linear matter density distribution for $k > 1h\,{\rm Mpc}^{-1}$ can be reconstructed using the halo model formalism. This is based on the assumption that all matter in the universe can be associated with collapsed and virialized haloes. In real space, the matter–matter correlation can be decomposed into two components:

$$\xi(r) = \xi_{\rm 1h}(r) + \xi_{\rm 2h}(r), \tag{16}$$

where $\xi_{\rm 1h}(r)$ and $\xi_{\rm 2h}(r)$ are one and two halo term components, that account for the matter–matter correlation in the same or in distant haloes, respectively. Following the halo model formalism as described by Cooray & Sheth (2002) and Giocoli et al. (2010b), we can relate real and Fourier, making explicit the redshift dependence, considering that

$$P(k,z) = 4\pi\int\xi(r,z)\frac{\sin(kr)}{kr}r^2{\rm d}r, \tag{17}$$

and write the one and two halo term in Fourier space as

$$P_{\rm 1H}(k,z) = \int_{M_{\rm min}}\left(\frac{M_{\rm h}}{\bar{\rho}}\right)^2 n(M_{\rm h},z) \times\int p(c_{\rm h}|M_{\rm h})u^2(k|c_{\rm h}(M_{\rm h}))\,{\rm d}c_{\rm h}\,{\rm d}M_{\rm h}, \tag{18}$$

$$P_{\rm 2H}(k,z) = P_{\delta,\rm lin}(k)\Big[\int_{M_{\rm min}}\frac{M_{\rm h}}{\bar{\rho}}n(M_{\rm h},z)\,b(M_{\rm h},z) \times\int p(c_{\rm h}|M_{\rm h})\,u(k|c_{\rm h},M_{\rm h})\,{\rm d}c_{\rm h}\,{\rm d}M_{\rm h}\Big]^2, \tag{19}$$

where $u(k|c_{\rm h}, M_{\rm h})$ represents the Fourier transform of the NFW matter density profile, $b(M_{\rm h}, z)$ the halo bias for which we use the model by Sheth & Tormen (1999), and $n(M_{\rm h}, z)$ the halo mass function for which we adopt the Despali et al. (2016) model that describes very well the mass function of PINOCCHIO light-cones, as can be noticed in Fig. 2. In the two equations above, we have made it explicit that the halo mass function is typically integrated from a given minimum halo mass $M_{\rm min}$ and that we use a stochastic model for the concentration mass relation with a scatter $\sigma_{\ln c} = 0.25$, as considered in WL-MOKA. It is worth mentioning that equation (19) needs to be normalized by

$$P_{\rm 2H,0}(k,z) = \left[\int_{M_{\rm min}}\frac{M_{\rm h}}{\bar{\rho}}n(M_{\rm h},z)\,b(M_{\rm h},z)\,{\rm d}M_{\rm h}\right]^2, \tag{20}$$

since it has to match the linear theory on large scales, i.e. for small k.

In Fig. 4, we show the halo model predictions for the convergence power spectra, at three different source redshifts (from bottom to

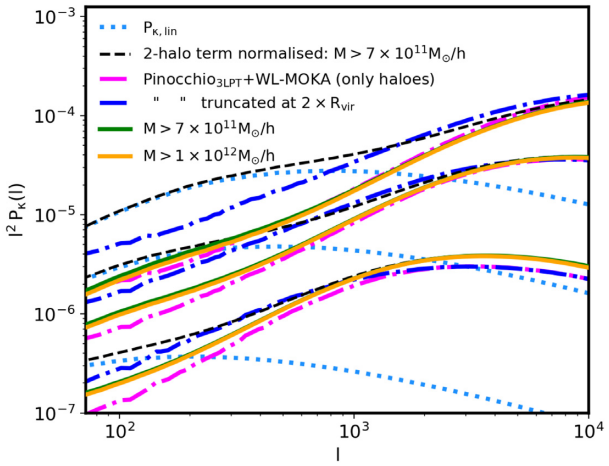

Figure 4. Convergence power spectrum prediction using halo model formalism. The black dashed curves show the prediction at three different fixed source redshifts using equation (15) (from bottom to top, $z = 0.5$, 1.4, and 4) where the lower limit of halo mass function integrals is $M_{\rm min} = 7 \times 10^{11}$ $\rm M_{\odot}\,\mathit{h}^{-1}$ and the two halo term has been normalized using equation (20) to match the linear prediction – dotted light blue curves. The magenta (blue) dot-dashed curves show the average measurements done on 512 convergence maps constructed combining PINOCCHIO PLC and WL-MOKA using only haloes (truncating the profile at two times the halo virial radius). The green and the orange curves display the analytical halo model prediction summing the contribution of equations (18) and (19), without normalizing the 2-halo term, for two different minimum halo masses.

top, $z = 0.5$, 1.4, and 4) integrating the matter power spectra as in equation (15). The black dashed curves show the prediction of the halo model summing the 1- and 2-halo term, with the latter normalized by the equation (20) to match on large scales the linear theory power spectra (dotted light blue lines). The magenta dot–dashed curves exhibit the average convergence power spectra of 512 maps constructed by WL-MOKA using haloes from the PINOCCHIO reference runs; for comparison, the blue dot–dashed curves display the results from the 512 maps created truncating the halo density profiles at two times the virial radius. Green and orange curves display the prediction of the 1- plus 2-halo term not normalized. The fact that the trend of those curves is similar as the PINOCCHIO plus WL-MOKA indicates that the convergence maps we have constructed using only haloes do not match the predictions from linear theory on large scale. In the analytic halo model formalism, this is compensated only in the 2-halo term, normalizing it by an effective bias contribution as in equation (20), without interferring on the matter density distribution on small scales as described by the 1-halo term. However, it is worth noticing that in the convergence maps constructed using WL-MOKA we cannot separate a priori the two terms; when including the unresolved matter contribution using linear theory, this will include somehow a small correlation between large and small scales compensating for rescaling the amplitude as in equation (14).

In Fig. 5, we display the relative differences, with respect to the case of $M_{\rm min} = 7 \times 10^{13}$ $\rm M_{\odot}\,\mathit{h}^{-1}$, of the total analytical halo model convergence power spectra, at the same three fixed source redshifts, assuming various minimum halo masses. While on the left-hand panel the 2-halo term is not normalized, in the right-hand panel equation (19) has been normalized by the effective bias term as in equation (20). In this latter case, we can notice that the mass resolution of the halo model integrals has a negligible effect on large scales, where the 2-halo term is forced to follow linear theory, while on small scales (large l) it manifests in appreciable differences.

3 RESULTS

In Fig. 6, we show the convergence power spectra at three source redshifts $z_{\rm s} = 4$, 1.4, and 0.5 from top to bottom, respectively. The dotted blue curves represent the predictions from linear theory using equation (15), the dot–dashed magenta ones the average convergence power spectra of the haloes over 512 different realizations of PINOCCHIO light-cones – left-hand panel of Fig. 3. The red (in particular this is a falu red) solid curves display the average power spectra of the 512 simulated convergence fields in which we include also the contribution from unresolved matter (central panel of Fig. 3), the shaded regions enclose the standard deviation of the various realizations. We remind the reader that while the numerical cosmological simulation has been run with only one IC displacement field, all 25 light-cones generated from this have been constructed by randomizing the simulation box by translating the particles and redefining the simulation centre when building-up the light-cones. In Fig. 7, we compare the convergence power spectra of our final maps (red solid curves) with the ones from the N-body simulation (green dots). From the figure we notice a very good agreement between our model and the N-body results up to $l \simeq 3 \times 10^3$ where the green data points start to deviate at low redshifts due to particle shot noise (Giocoli et al. 2016), and the model tends to move down because of the absence of concentrated low-mass haloes below the numerical resolution. The black dashed curves show the corresponding convergence power spectra obtained by integrating the non-linear matter spectra implemented in CAMB by Takahashi et al. (2012). In the bottom sub-panel, we display the relative difference between the N-body predictions and the approximate methods with respect to the non-linear projected matter power spectrum. From the figure, we can see that the non-linear predictions are recovered with percent accuracy from $l = 72$ (which is the angular mode corresponding to 5 deg) to $l = 3 \times 10^3$ (the largest mode expected to be covered by future wide-field surveys) using our approximate methods.

3.1 Stability with minimum halo mass

We profit from the large statistic samples available from the PINOCCHIO runs and we investigate how the reconstruction (Giocoli et al. 2017) of large-scale projected power missing from haloes behaves, as a function of redshift, when a higher threshold for minimum halo mass is used. We run our WL-MOKA pipeline adopting different threshold for the minimum halo mass. In Fig. 8, we display the convergence map for $z_{\rm s} = 1.4$ constructed with a minimum halo mass of 7×10^{11}, 10^{12}, 10^{13}, and 10^{14} $\rm M_{\odot}\,\mathit{h}^{-1}$ from left to right, respectively. The value of 7×10^{11} $\rm M_{\odot}\,\mathit{h}^{-1}$ corresponds to our minimum halo mass in the $\rm PINOCCHIO_{3LPT}$ reference run, while the case with minimum mass of 10^{14} $\rm M_{\odot}\,\mathit{h}^{-1}$ will help us in better understanding the contribution of galaxy cluster size haloes to the weak lensing signal. In the figure, top and bottom panels display the halo and the total contributions to the convergence, respectively. In the latter case, we add the linear matter density contribution due to unresolved matter below the corresponding mass threshold limit. From the figure, we notice that while clusters represent the high-density peaks of the convergence field, smaller mass haloes trace the filamentary structure of the matter density distribution and contribute, in projection, to increasing the lensing signal (Martinet et al. 2018; Giocoli et al. 2018; Shan et al. 2018).

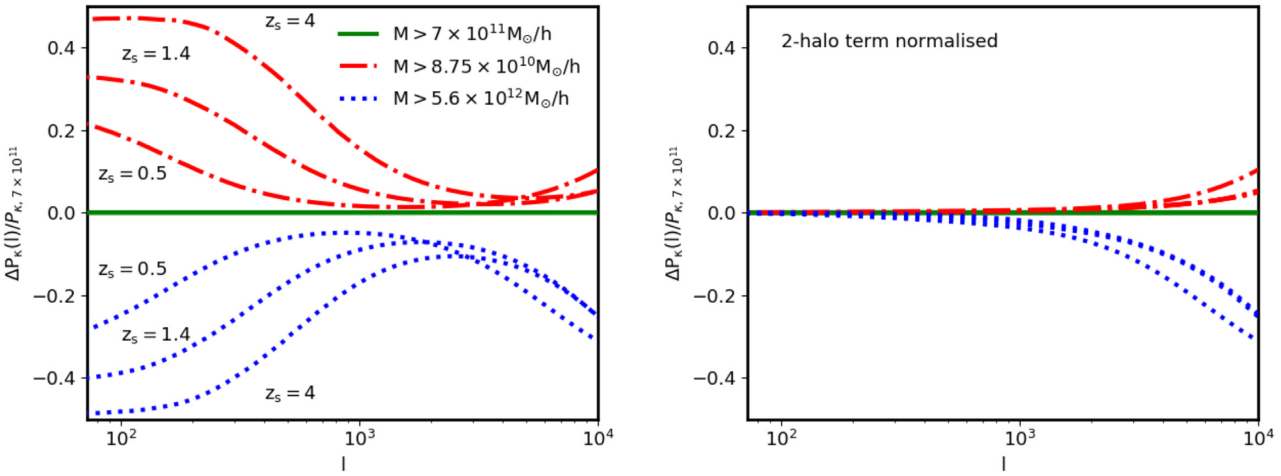

Figure 5. Relative difference of the convergence power spectra, computed using the halo model at three different fixed source redshifts, using different minimum halo mass threshold in the integrals. Left-hand panel shows the relative difference with respect to the prediction of the mass resolution of the reference run of the 1- and 2-halo terms summing the contributions from equation (15) of the expressions in equations (18) and (19). Right-hand panel displays the relative difference of the total contributions where the 2-halo term has been normalized by equation (20).

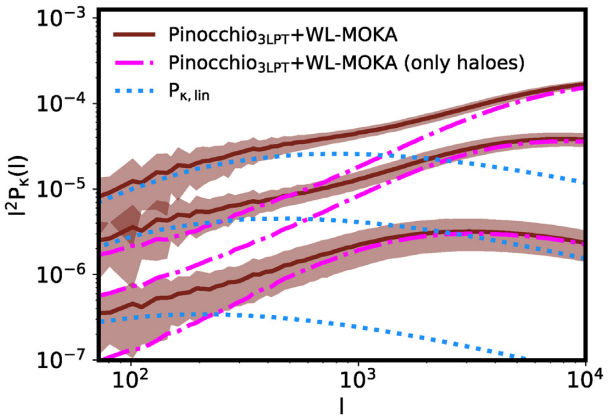

Figure 6. Convergence power spectra at three different source redshifts: from top to bottom $z_s = 4$, 1.4, and 0.5. The dotted blue curves display the predictions using linear power spectrum, dot–dashed purple the average halo contribution of 512 light-cones from PINOCCHIO. The red lines are the average measurements of 512 realizations of the convergence field from haloes and diffuse component, the shaded regions enclose the rms of the various realizations.

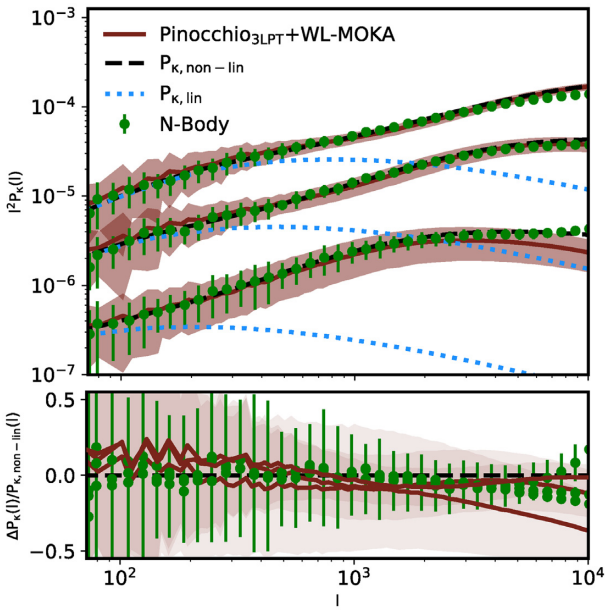

Figure 7. Convergence power spectra at three different source redshifts, from top to bottom $z_s = 4$, 1.4, and 0.5. We compare the predictions using approximate methods PINOCCHIO and WL-MOKA (solid red curves) with measurements from light-cones extracted from a cosmological *N*-body simulation using MAPSIM. Black dashed and blue dotted curves display the predictions using linear and non-linear power spectra from CAMB, the latter refers to the implementation by Takahashi et al. (2012). In the bottom sub-panel, we display the relative differences of the *N*-body and the approximate convergence power spectra with respect to the non-linear predictions.

In Fig. 9, we present the relative difference of the average convergence power spectra, for 512 different realizations, as computed from the different mass threshold maps with respect to the reference one, that has a mass resolution of $7 \times 10^{11}\,\mathrm{M}_\odot\,h^{-1}$. Panels from left to right consider different fixed source redshift $z_s = 0.5$, 1.4, and 4, respectively; while on the top we show only the halo contributions. In the bottom, we account also for the contribution from unresolved matter. These figures help us to quantify the contribution of various haloes to the convergence power spectra. In particular, from the top panels we can notice that the contribution of clusters evolves with the redshift going from an average value of approximately 40 per cent for sources at $z_s = 0.5$ to 10 per cent for $z_s = 4$. This is an effect where the cluster contribution is modulated by the lensing kernel, depending on the considered source redshift, and it is sensitive to the redshift evolution of the cluster mass function. On the other side, in the bottom panels we can notice that the average power spectra from total effective convergence maps built using only clusters deviates by approximately 30 per cent with respect to the reference ones, independently of the source redshift. The yellow shaded region, in the right part of each panel, indicates where future wide-field surveys like the ESA Euclid mission will not be able to

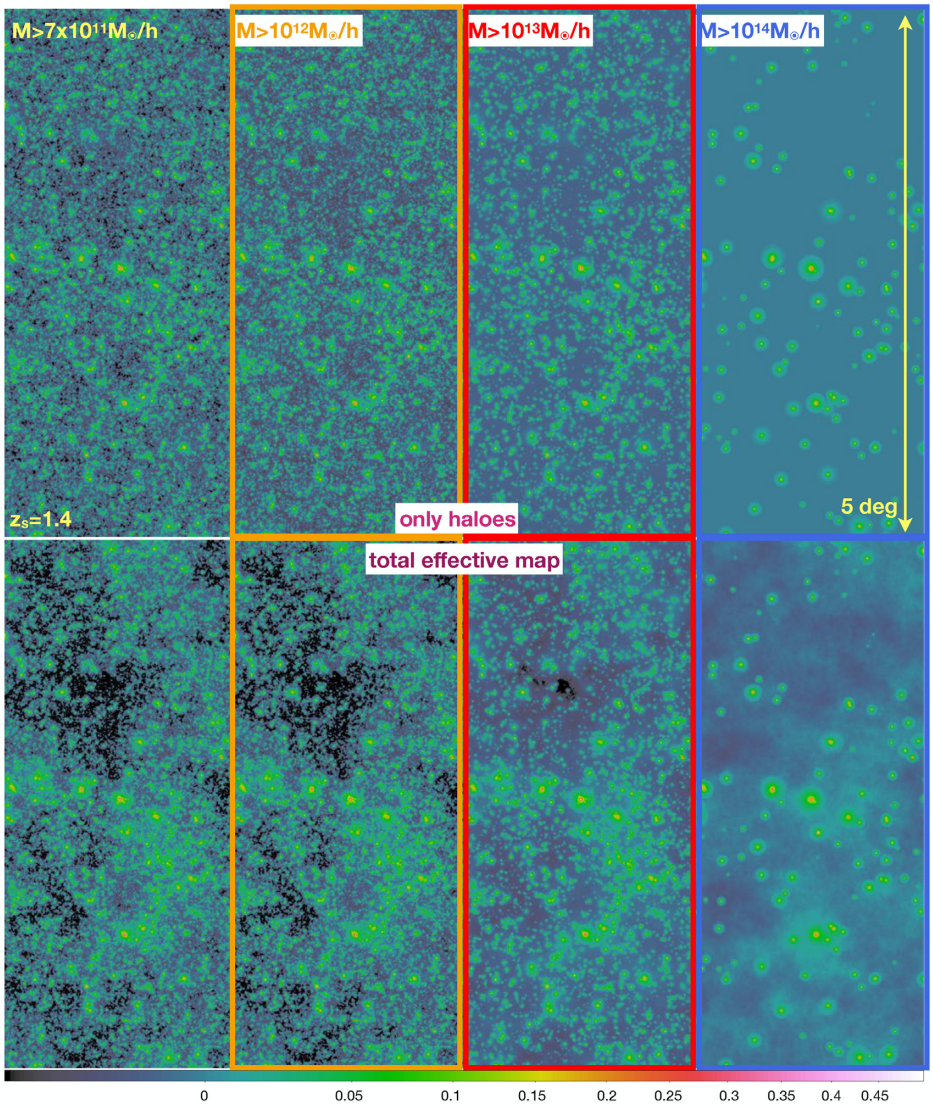

Figure 8. Convergence maps for $z_s = 4$ constructed adopting different minimum mass thresholds: we use all haloes with mass larger than 7×10^{11}, 10^{12}, 10^{13} and $10^{14}\,M_\odot\,h^{-1}$ from left to right, respectively. The top panels show the halo contribution while the bottom ones include also the linear contribution coming from unresolved matter, below the considered minimum halo mass.

provide any reliable data; future wide-field missions will be able to probe the convergence power spectrum up to $l \approx 3 \times 10^3$.

As discussed by Munari et al. (2017) and Paranjape, Sheth & Desjacques (2013) in PINOCCHIO, the bias of dark matter haloes is a prediction. This applies also when the code is interfaced with WL-MOKA in creating effective convergence maps. In particular, the square-root of the ratio at large angular scales (the comoving scale of $k = 0.1h$ Mpc^{-1} corresponds approximately to $l \approx 150$, 300, and 520 for source redshift $z_s = 0.5$, 1.4, and 4, respectively) between the halo and the total convergence power spectrum gives us a measure of the projected halo bias. This can be modelled using the 2-halo term of the projected halo model as discussed in Section 2.3.

3.2 LPT order for the displacement fields

As presented by Munari et al. (2017), in the new version of PINOCCHIO the user can run the code adopting different LPT orders for particle displacement fields: ZA, 2LPT, and 3LPT. In this section, we investigate how the reconstructed convergence power spectra, at different fixed source redshifts, depend on the adopted displacement order. In Fig. 10, we show the relative difference of the convergence power spectra at three source redshifts. Blue dashed and green dotted curves display the relative difference of the ZA and 2LPT cases with respect to the 3LPT. While the top panels exhibit the power spectra due only to resolved haloes in the light-cone simulations, the bottom ones account also for the corresponding contribution due to matter among haloes. In the bottom panels, where we have the total contribution, while the 2LPT case differs from the 3LPT case by less than 1 per cent, the ZA case tends to deviate more than $5 - 7$ per cent with larger deviations for larger angular modes (small scales) reaching values of ~ 10 per cent. We remind the reader that the average measurements are done only on 25 different light-cone runs and the simulations, with various displacement prescription, share the same seeds and phases, when generating the ICs.

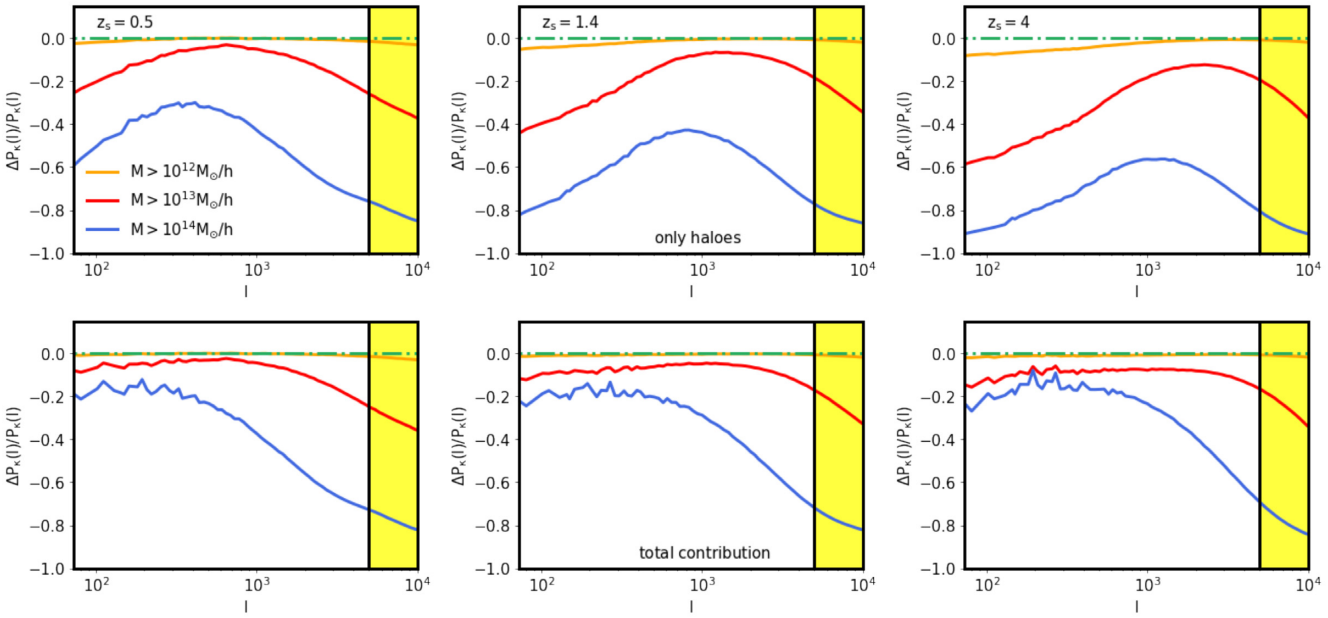

Figure 9. Relative difference in the convergence power spectra adopting various minimum halo mass thresholds at three different source redshifts: $z_s = 0.5$, 1.4, and 4 from left to right, respectively. Orange, red, and blue curves display the measurements considering minimum masses of 10^{12}, 10^{13}, and 10^{14} $M_\odot\, h^{-1}$ with respect to the reference case that has a minimum halo mass of 7×10^{11} $M_\odot\, h^{-1}$. As in Fig. 8, the top panels show the average contribution of 512 realizations constructed using only haloes while the bottom ones show the average including also the linear contribution coming from unresolved matter, below the considered minimum halo mass. The yellow shaded region marks the region of $l > 5 \times 10^3$ rad, up to which future wide-field surveys are expected to measure the weak lensing convergence power spectra (Laureijs et al. 2011).

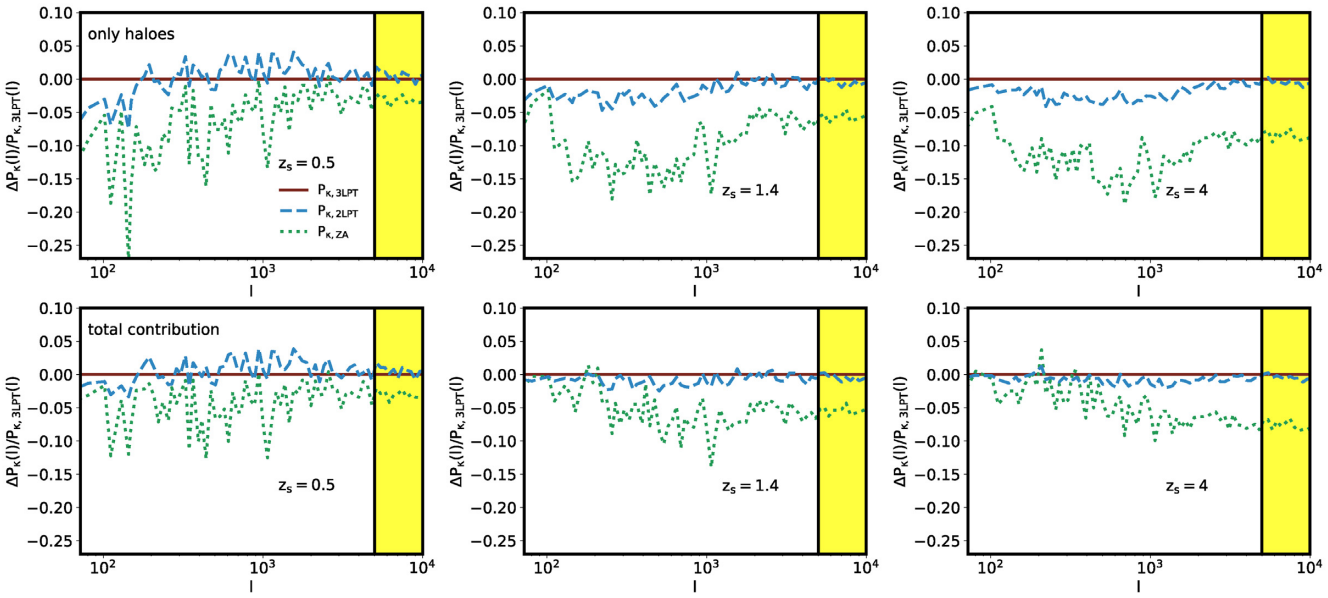

Figure 10. Relative convergence power spectra between maps constructed using PINOCCHIO 2LPT (dashed blue) and ZA (dotted green) with respect to 3LPT. From left to right, we show the cases for the three considered source redshifts: $z_s = 0.5$, 1.4, and 4, respectively. Top and bottom panels show the cases in which the maps are constructed using only haloes or haloes plus diffuse matter.

3.3 Resolution of approximate method simulations

The reconstructed 2D field using the halo model technique depends also on the resolution of the grid mesh on the top of which the halo catalogue is constructed in the PLC. As for numerical simulations that solve the full *N*-body relations, PINOCCHIO runs are much faster when the displacement grid is coarser. In Fig. 11, we show the case in which we compare the convergence power spectra of 512 approximate method PLCs with grid resolution of 512^3 and our reference run of 1024^3; in both cases we assume a 3LPT displacement field and the same initial seeds for the ICs. The orange curves display the relative difference of the 1024^3

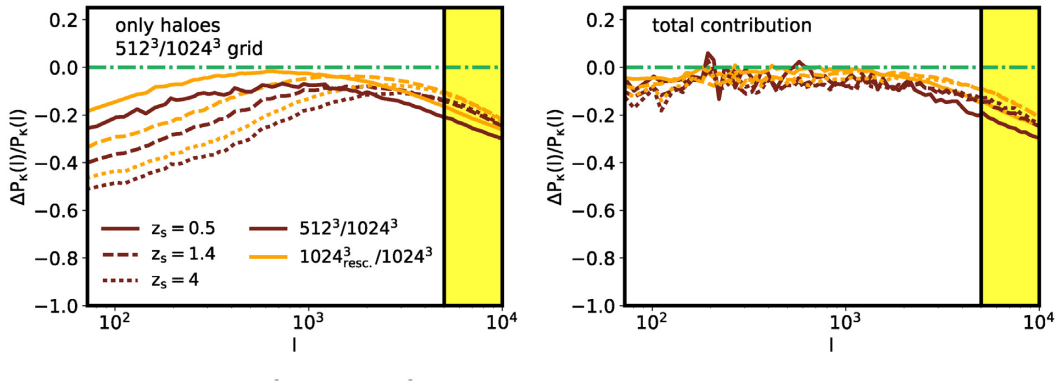

Figure 11. Relative difference between the 512^3 and the 1024^3 simulations. The different curves show the results for the three source redshifts, left-hand and right-hand panels refer to the case where we consider the contribution only from haloes or we include also the diffuse matter using linear theory, respectively. The orange curves display the relative difference when building the maps from the 1024^3 we adopt the same minimum halo mass resolution of the 512^3, namely $5.6 \times 10^{12}\,\mathrm{M}_\odot\,h^{-1}$.

maps rescaled to the same resolution of the 512^3 with respect to the reference resolution run. Left-hand and right-hand panels show the comparison of the power spectra coming only from the haloes and from the full projected matter density distribution (haloes plus unresolved matter treated using linear theory). From the left figure we can see that the runs with lower resolution have a redshift dependence trend at low angular modes (larger scales). These are integrated effects due to the haloes that mainly contribute to the lensing signal when accounting for the lensing kernel at a given source redshift. However, from the right figure we can notice that when adding the contribution coming from unresolved matter using linear theory (right-hand panel) this redshift tendency disappears, and on average up to $l = 3 \times 10^3$ the relative difference of the low-resolution run is between 5 and 10 per cent. At those scales it is evident that the simulations constructed from the coarser grid are missing concentrated small haloes. In rescaling the 1024^3 to the same map resolution of the 512^3, namely $5.6 \times 10^{12}\,\mathrm{M}_\odot\,h^{-1}$, we notice few percent deviations probably attributed to the different displacement grids of the two runs, halo finding threshold resolution when linking particles in FoF and halo bias that enter on the 2-halo term on large scale, even if the two PLC have the same minimum halo mass.

Fig. 12 displays the relative difference between full power spectra of 25 high-resolution and reference runs that share the same IC seeds. As in the previous figures, the different line types refer to various fixed source redshifts. As we can read from Table 1, the run with 2048^3 grid mesh has a minimum halo mass a factor of 8 lower than the one with 1024^3. The figure shows that convergence power spectra computed from the high-resolution runs are approximately 3–5 per cent higher that the ones from our reference simulations. This difference probably arises from the fact that when including the contribution from diffuse matter in our convergence halo maps we are not able to specifically separate the 1- and 2-halo term – as we do analytically in the halo model as discussed in Section 2.3, causing a small shift up. However, we want to underline that the main goal of our approach is to be able to build a fast and self-consistent method for covariances; many faster and more accurate approaches already exist in term of non-linear power spectra that will be used for modelling the small scales observed signals from future weak lensing surveys (Peacock & Dodds 1996; Smith et al. 2003; Takahashi et al. 2012; Debackere, Schaye & Hoekstra 2020; Schneider et al. 2020).

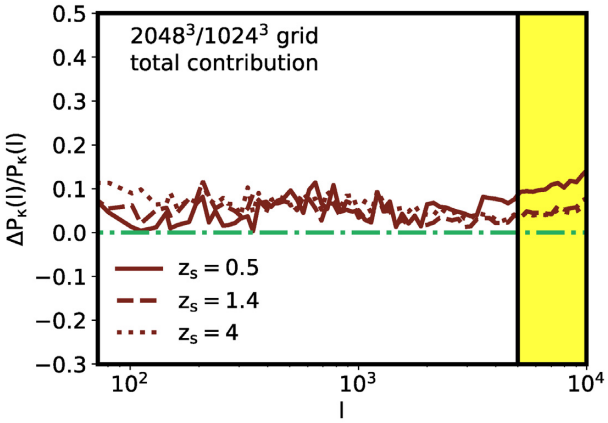

Figure 12. Relative difference between the convergence power spectra in the 2048^3 and 1024^3 runs. The relative difference has been computed as average of 25 difference PLC realizations considering both haloes and diffuse matter.

For summary, we address the reader to Appendix B where we show the convergence maps build using different particle and grid resolutions, while adopting the same initial displacement seed and phases. The maps refer to light-cones build only from haloes up to $z_s = 1.4$.

In Fig. 13, we show the relative difference of the average power spectra computed from 512 different PLCs with 1024^3 grid mesh with respect to the prediction obtained integrating the non-linear matter power spectrum from CAMB using the Takahashi et al. (2012) implementation. The dark grey, grey, and light grey regions mark the relative difference of 5, 15, and 25 per cent, blue data points with the corresponding error bars are the convergence power spectra prediction obtained by Izard, Fosalba & Crocce (2018) using ICE-COLA with respect to the MICE simulation for sources at $z_s = 1$. These comparisons strengthen the power of the two methods PINOCCHIO plus WL-MOKA in reconstructing the projected non-linear power spectrum, and the flexibility to use different fixed source redshifts or a defined source redshift distribution of sources. The limit of these runs are related to the small field of view we have decided to simulate, but this will be extended in a future dedicated

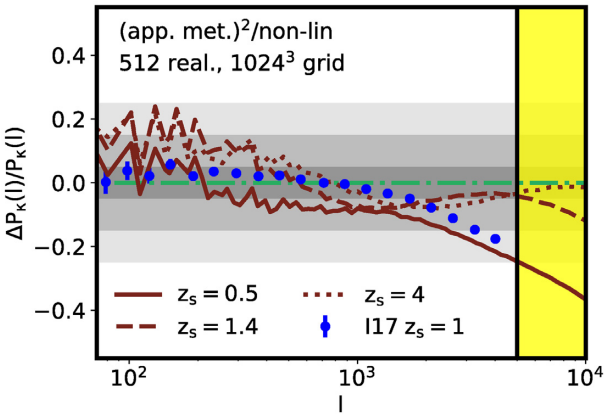

Figure 13. Relative difference between convergence power spectra computed using approximate methods and the prediction from non-linear matter power spectrum as implemented in CAMB by Takahashi et al. (2012). The different curves show the results for the three considered source redshifts, while the data points display the results obtained by Izard et al. (2018) for $z_s = 1$ comparing their approximate methods for weak lensing, based on ICE-COLA, with respect to the reference MICE simulation. In the figure, the red curves show the average values obtained on 512 PINOCCHIO light-cone realizations with a grid resolution of 1024^3. Dark grey, grey, and light grey bands indicate 5, 15, and 25 per cent relative differences.

work as well as the possibility to construct convergence on HEALPIX[6] maps.

The inference for cosmological parameters, expressed in term of the data vector $\vec{\Theta}$, using weak gravitational lensing is found by minimizing the likelihood function that compares observational data to reference models (Simon, King & Schneider 2004; Takada & Jain 2004; Kilbinger et al. 2013; Kitching et al. 2014; Köhlinger et al. 2017). In the case of Gaussian distributed data, the likelihood can be approximated as

$$\ln \mathcal{L}(\vec{\Theta}) \propto -\frac{1}{2}\sum_{i,j=1}^{N_b}\left[P_\kappa^{\text{'obs'}}(l_i) - P_\kappa(l_i,\vec{\Theta})\right] M(l_i,l_j)^{-1} \times \left[P_\kappa^{\text{'obs'}}(l_j) - P_\kappa(l_j,\vec{\Theta})\right], \quad (21)$$

where $M(l,l')$ represents the covariance matrix; its inverse is usually termed precision matrix. It is worth noting that in the equation above, we have neglected the cosmological dependence of the covariance matrix. However, this is the subject of ongoing study and discussion (Labatie, Starck & Lachièze-Rey 2012; Harnois-Déraps, Giblin & Joachimi 2019) and we plan to address it in a future work focused both on clustering and weak gravitational lensing.

Using different weak lensing light-cone realizations, we can build the covariance matrix as

$$M(l,l') = \langle (P_\kappa(l) - \bar{P}_\kappa(l))(P_\kappa(l') - \bar{P}_\kappa(l'))\rangle, \quad (22)$$

where $\langle \bar{P}_\kappa(l)\rangle$ represents the best estimate of the power spectrum at the mode l obtained from the average, or the median, of all the corresponding light-cone realizations and $P_\kappa(l)$ represents the measurement of one realization. The matrix is then normalized as follows:

$$m(l,l') = \frac{M(l,l')}{\sqrt{M(l,l)M(l',l')}}, \quad (23)$$

[6]https://healpix.jpl.nasa.gov

in order to be unity on the diagonal. The covariance matrix constructed in this way accounts both for a Gaussian and non-Gaussian contribution arising from mode coupling due to non-linear clustering and for the survey geometry (Scoccimarro, Zaldarriaga & Hui 1999; Cooray & Hu 2001; Harnois-Déraps, Vafaei & Van Waerbeke 2012; Sato & Nishimichi 2013). Off-diagonal terms with value near unity indicate high correlation while values approaching zero indicate no correlation. The covariance matrices using the convergence power spectra of the maps generated using PLC halo catalogues from PINOCCHIO account for correlation between observed modes and those with wavelength larger than the simulated field of view, or survey size. In fact (i) the simulations have 1 Gpc h^{-1} comoving box side, (ii) the simulated convergence maps have been constructed from a cone with aperture 7.2 deg, and (iii) each PLC halo catalogue, produced using PINOCCHIO, originated from a different IC realization. We underline also that our covariances do not account for any noise nor systematic errors that typically enter in the uncertainty budget for the cosmological forecasts (Fu et al. 2008; Hildebrandt et al. 2017).

The top panels of Fig. 14 show the covariance matrix for the convergence power spectra computed from our reference 512, 1024^3 mesh grid considering the 3LPT method to displace halo and particle positions. The three panels refer to the covariances for sources at $z_s = 0.5$, 1.4, and 4 from left to right, respectively. From the figure we note very good quantitative agreement with the results that have been presented on the same field of view (Giocoli et al. 2017) and qualitatively with the covariances computed by Giocoli et al. (2016) on the BigMultiDark (Prada et al. 2016) light-cones that have a rectangular geometry matching the W1 and W4 VIPERS fields (Guzzo et al. 2014). In Appendix A, we show the covariance matrices, at the same three fixed source redshifts, using only haloes, in building the different convergence maps, which display appreciable differences – with respect to the ones presented here – mainly for sources at higher redshifts. In the bottom panels of Fig. 14, we display the signal to noise of the diagonal terms of various covariances, for comparison purpose. The green dashed curves refer to the realizations obtained from 25 convergence maps of our reference *N*-body simulation, the solid blue and cyan curves represent the ones obtained from 512 runs of PINOCCHIO halo catalogues plus WL-MOKA adding or not the diffuse matter component among haloes using linear theory predictions, respectively. In the central panel (the closest source redshift to the mean of the redshift distribution useful from weak lensing expected from future wide-field-surveys), we show the Gaussian covariance (orange dot–dashed) – obtained running 10 000 Gaussian realization of the convergence power spectrum – and the (dotted magenta) contribution due to the discrete number density of background sources (Refregier et al. 2004) adopting a Euclid-like sky coverage of 15 000 sq. degs. and 30 galaxies per square arcmin. From the figure we can notice that the diagonal term of the covariance computed from 512 PINOCCHIO PLC halo catalogues (blue solid curve) is at large scale in agreement with the full ray-tracing simulations while at small scales it moves up dominated by sample variances (Barreira, Krause & Schmidt 2018a,b). All 512 runs have different ICs, while the 25 full ray-tracing convergence maps are extracted from the same simulation with fixed IC. At large angular modes the blue curves move down because of a smaller number of PLC realizations.

A systematic comparison of the off-diagonal term contributions of the covariance, for $z_s = 1.4$, is displayed in Fig. 15. In the left-hand panel, we show the terms at two fixed values for l' of the covariances computed (blue curves) using 512 realization maps

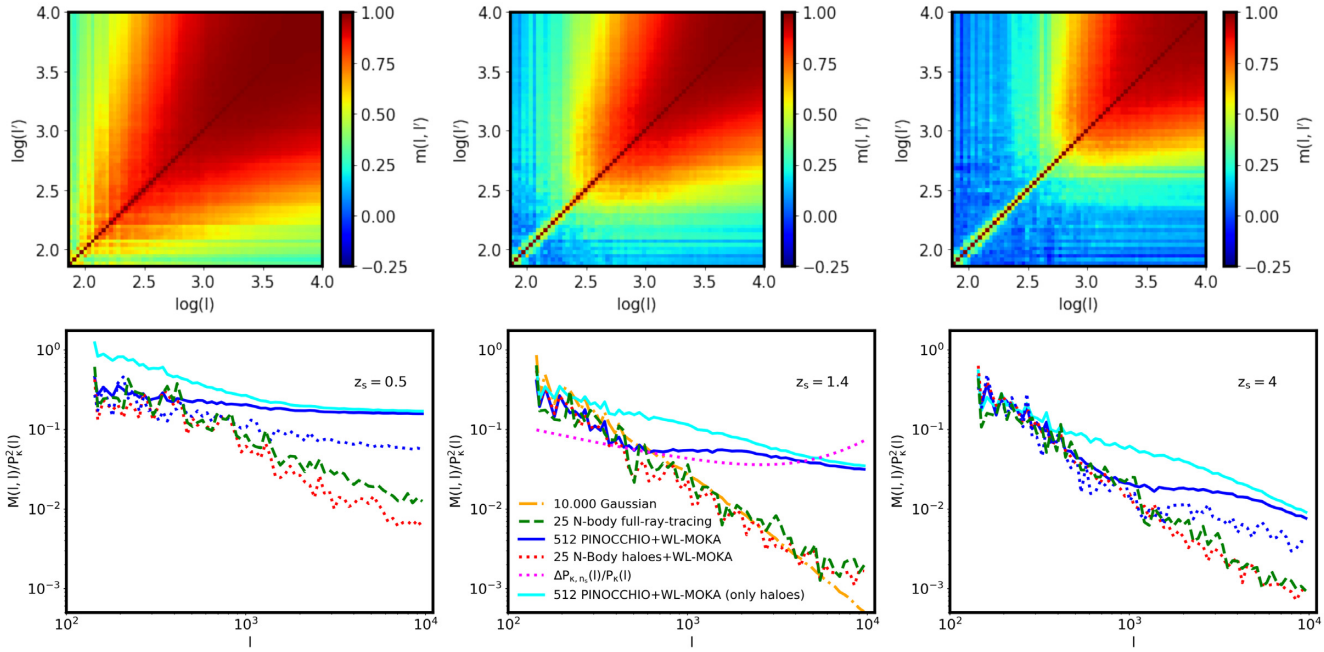

Figure 14. Top panels: weak lensing covariance matrices for $z_s = 0.5$, 1.4, and 4 from left to right, respectively, constructed from 512 PLC PINOCCHIO simulations – 3LPT runs with a grid of 1024^3 – and using our fast weak lensing halo model WL-MOKA. The aperture of the field of view is set to 5 deg on a side and convergence maps are resolved with 2048^2 pixels. Bottom panels: signal to noise of the diagonal term of different covariance matrices. In the central panel (the closest to the mean of the source redshift distribution useful from weak lensing expected from future wide-field-survey), we display also the result from Gaussian covariance (dash–dotted orange curve) and from the observational discrete number density of background sources (Refregier et al. 2004) adopting a Euclid-like sky coverage of 15 000 sq. degs. and 30 galaxies per square arcmin (dotted magenta).

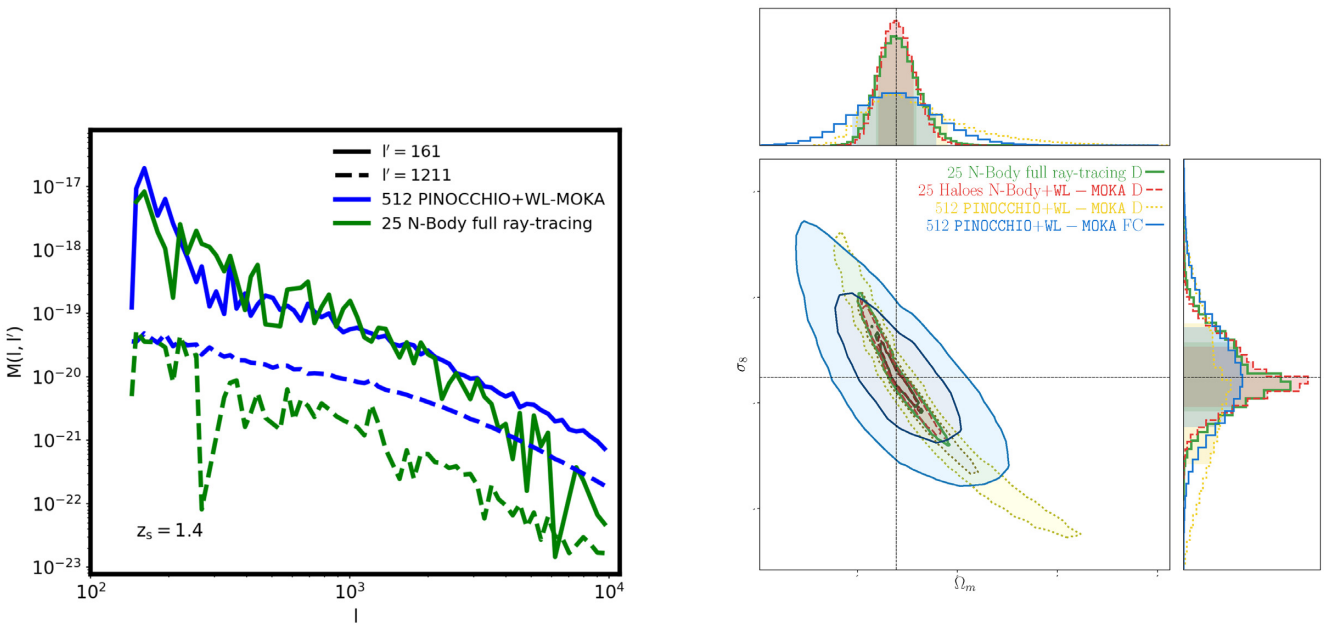

Figure 15. Left-hand panel: Comparison between off-diagonal covariance matrix terms, at two fixed values for l', computed from 25 *N*-body full ray-tracing simulations and 512 simulations obtained using the approximate methods for $z_s = 1.4$. Right-hand panel: 1σ and 2σ cosmological constraints in the Ω_m-σ_8 parameter space computed adopting different covariances for $z_s = 1.4$. Green and red contours adopt the diagonal term of the covariances constructed from 25 *N*-body convergence map realizations using particle full ray-tracing and halo population plus WL-MOKA as in Giocoli et al. (2017), respectively. The yellow and blue contours make use of the covariance from 512 approximate methods convergence maps: considering only the diagonal (D) or the full covariance (FC), respectively. Being interested in the relative performances of the various covariance terms, we follow the same approach as in Krause & Eifler (2017) not including the axis values.

adopting our approximate methods and (green curves) employing 25 full ray-tracing maps from our reference *N*-body simulation. From the figure, we notice that for intermediate values for l' the two covariances are relatively comparable, while for larger values of l they deviate mainly due to both numerical resolution and particle noise contributions. As underlined in Giocoli et al. (2017), the full ray-tracing covariances are quite noisy and problematic to be inverted when used to constrain cosmological parameters. In the right-hand panel, we show the cosmological constraints obtained adopting various covariances in the $\Omega_{\rm m}$-σ_8 parameter space. The results refer again to $z_{\rm s} = 1.4$. Since the aim of this test is to display the relative performances of the various covariance terms, we follow the same approach as in Krause & Eifler (2017) not including the axis values. A self-consistent analysis to constraint cosmological parameters from weak lensing data sets could not neglect shape measurements inaccuracy (Bernstein & Jarvis 2002; Kacprzak et al. 2012; Miller et al. 2013), photometric redshift errors, and uncertainties of the reconstructed source redshift distribution (Hildebrandt et al. 2012; Benjamin et al. 2013; Yao et al. 2019; Wright et al. 2020). The green and red contours show the cosmological constraints derived when adopting the covariance matrices constructed from 25 realizations of the projected density field up to $z_{\rm s} = 4$ using full ray-tracing particle simulations and the halo catalogues plus WL-MOKA as in Giocoli et al. (2017), respectively. Since the covariance matrix from 25 full ray-tracing simulations is noisy we could use only the diagonal (D) term. We underline that the Gaussian covariance gives similar constraints to the green contours, not shown to avoid overcrowding the figure. The yellow contours show the constraints derived when using the diagonal term of the covariance constructed from 512 approximate method simulations, while the blue ones adopt the full covariance matrix, which exhibit a degradation of the figure of merit. The cosmological constraints have been obtained implementing the modelling of the cosmic shear power spectrum in the CosmoBolognaLib (Marulli, Veropalumbo & Moresco 2016) and accounting for the number of realizations when constructing the covariance as described by Hartlap, Simon & Schneider (2007) and Percival et al. (2014). We remind the reader that the use of these approximate covariances for analysing existing and future wide-field surveys will require more consistent tests with theoretical models, path we are currently pursuing inside different collaborations.

4 SUMMARY AND CONCLUSIONS

In this paper, we have presented a natural extension of the approximate Lagrangian perturbation theory code PINOCCHIO dedicated to creating fast and accurate convergence maps for weak gravitational lensing simulations. Since the methods implemented are quite general they constitute a tool for full cosmological analysis of observational data sets going from galaxy clustering to cluster counts and clustering to cosmic shear.

The main points of this work are:

(i) the halo mass function in PINOCCHIO PLCs is in very good agreement with both numerical simulation data and theoretical models with which we compare to;

(ii) the expected convergence power spectra constructed from our reference runs using only haloes, present within the PLC, are quite well recovered on small scales, however, we need to include also the contribution from matter present outside haloes to fully reconstruct the large scale modes as predicted from linear theory, this has been discussed and motivated with a dedicated comparison with the analytical halo model for non-linear power spectrum;

(iii) the full convergence maps have a power spectrum that is in agreement well within 5 per cent of that obtained from full ray-tracing through light-cones constructed from the reference cosmological *N*-body simulation;

(iv) the contribution of galaxy clusters to the total convergence power spectra at different source redshifts for $l < 3 \times 10^3$ remains constant, deviating approximately by 30 per cent with respect to the total ones, with a slight evolution with redshift due to the rarity of clusters at large look back times;

(v) the weak lensing power spectra obtained running PINOCCHIO with 2LPT displacement and then WL-MOKA agree within 1 per cent with the 3LPT reference run, however, when using ZA the projected power spectra deviate more than 7 per cent on large angular modes;

(vi) the relative differences between the convergence power spectra of our fast methods for weak lensing with respect to the reference measurements from *N*-body simulations is well below 5 per cent, consistent with what has been found also by other approximate methods;

(vii) the speed of our algorithms allows for the possibility of generating a very large number of light-cone weak lensing simulations and the opportunity to construct self-consist covariances for weak gravitational lensing.

A fast and accurate method for generating convergence maps using approximate methods is needed in light of the expected data from future wide-field surveys. In this work, we have presented the interfacing of PINOCCHIO and WL-MOKA that enables them to simulate cosmic shear signals from LSS. This adds a new capacity to PINOCCHIO, beyond the halo mass function and clustering, applicable to simulate quickly and consistently various covariances for different statistics, opening a new window for robust cosmological analyses of future observational data sets.

ACKNOWLEDGEMENTS

CG and MB acknowledge support from the Italian Ministry for Education, University and Research (MIUR) through the SIR individual grant SIMCODE, project number RBSI14P4IH. We acknowledge the grants ASI n. I/023/12/0, ASI-INAF n. 2018-23-HH.0, and PRIN MIUR 2015 Cosmology and Fundamental Physics: illuminating the Dark Universe with Euclid. CG, LM, and MM are also supported by PRIN-MIUR 2017 WSCC32 'Zooming into dark matter and proto-galaxies with massive lensing clusters'. TC is supported by the INFN INDARK PD51 grant. We acknowledge the anonymous reviewer for his/her useful comments that helped in improving the presentation of our methods and results. CG is grateful to Alex Barreira, Sofia Contarini, Wolfgang Enzi, Federico Marulli, and Alfonso Veropalumbo for helpful discussions and comments.

REFERENCES

Baldi M., 2012, MNRAS, 422, 1028
Baldi M., Pettorino V., Robbers G., Springel V., 2010, MNRAS, 403, 1684
Barreira A., Krause E., Schmidt F., 2018a, J. Cosmol. Astropart. Phys., 2018, 015
Barreira A., Krause E., Schmidt F., 2018b, J. Cosmol. Astropart. Phys., 2018, 053
Bartelmann M., 1996, A&A, 313, 697
Bartelmann M., Schneider P., 2001, Phys. Rep., 340, 291
Baugh C. M., 2006, Rep. Prog. Phys., 69, 3101

Benjamin J. et al., 2013, MNRAS, 431, 1547
Bennett C. L. et al., 2013, ApJS, 208, 20
Bergamini P. et al., 2019, A&A, 631, A130
Bernstein G. M., Jarvis M., 2002, AJ, 123, 583
Beutler F. et al., 2014, MNRAS, 443, 1065
Bond J. R., Cole S., Efstathiou G., Kaiser N., 1991, ApJ, 379, 440
Bullock J. S., Kolatt T. S., Sigad Y., Somerville R. S., Kravtsov A. V., Klypin A. A., Primack J. R., Dekel A., 2001, MNRAS, 321, 559
Carbone C., Petkova M., Dolag K., 2016, J. Cosmol. Astropart. Phys., 2016, 034
Castorina E., Sefusatti E., Sheth R. K., Villaescusa-Navarro F., Viel M., 2014, J. Cosmol. Astropart. Phys., 2014, 49
Castro T., Quartin M., Giocoli C., Borgani S., Dolag K., 2018, MNRAS, 478, 1305
Chen Y., Mo H. J., Li C., Wang H., Yang X., Zhang Y., Wang K., 2020, preprint (arXiv:2003.05137)
Cole S. et al., 2005, MNRAS, 362, 505
Cooray A., Hu W., 2001, ApJ, 554, 56
Cooray A., Sheth R., 2002, Phys. Rep., 372, 1
De Boni C., Serra A. L., Diaferio A., Giocoli C., Baldi M., 2016, ApJ, 818, 188
Debackere S. N. B., Schaye J., Hoekstra H., 2020, MNRAS, 492, 2285
Despali G., Giocoli C., Angulo R. E., Tormen G., Sheth R. K., Baso G., Moscardini L., 2016, MNRAS, 456, 2486
Dolag K., Bartelmann M., Perrotta F., Baccigalupi C., Moscardini L., Meneghetti M., Tormen G., 2004, A&A, 416, 853
Duffy A. R., Schaye J., Kay S. T., Dalla Vecchia C., 2008, MNRAS, 390, L64
Eisenstein D. J. et al., 2005, ApJ, 633, 560
Erben T. et al., 2013, MNRAS, 433, 2545
Fu L. et al., 2008, A&A, 479, 9
Gao L., Navarro J. F., Cole S., Frenk C. S., White S. D. M., Springel V., Jenkins A., Neto A. F., 2008, MNRAS, 387, 536
Giocoli C., Moreno J., Sheth R. K., Tormen G., 2007, MNRAS, 376, 977
Giocoli C., Tormen G., van den Bosch F. C., 2008, MNRAS, 386, 2135
Giocoli C., Tormen G., Sheth R. K., van den Bosch F. C., 2010a, MNRAS, 404, 502
Giocoli C., Bartelmann M., Sheth R. K., Cacciato M., 2010b, MNRAS, 408, 300
Giocoli C., Meneghetti M., Bartelmann M., Moscardini L., Boldrin M., 2012a, MNRAS, 421, 3343
Giocoli C., Tormen G., Sheth R. K., 2012b, MNRAS, 422, 185
Giocoli C., Marulli F., Baldi M., Moscardini L., Metcalf R. B., 2013, MNRAS, 434, 2982
Giocoli C., Metcalf R. B., Baldi M., Meneghetti M., Moscardini L., Petkova M., 2015, MNRAS, 452, 2757
Giocoli C. et al., 2016, MNRAS, 461, 209
Giocoli C. et al., 2017, MNRAS, 470, 3574
Giocoli C., Moscardini L., Baldi M., Meneghetti M., Metcalf R. B., 2018, MNRAS, 478, 5436
Guzzo L. et al., 2014, A&A, 566, A108
Harnois-Déraps J., Vafaei S., Van Waerbeke L., 2012, MNRAS, 426, 1262
Harnois-Déraps J., Giblin B., Joachimi B., 2019, A&A, 631, A160
Hartlap J., Simon P., Schneider P., 2007, A&A, 464, 399
Hilbert S. et al., 2020, MNRAS, 493, 305
Hildebrandt H. et al., 2012, MNRAS, 421, 2355
Hildebrandt H. et al., 2017, MNRAS, 465, 1454
Hockney R. W., Eastwood J. W., 1988, Computer Simulation Using Particles, Hilger, Bristol
Ivezic Z. et al., 2009, in American Astronomical Society Meeting Abstracts #213 Vol. 41 of Bulletin of the American Astronomical Society. p. 366
Izard A., Fosalba P., Crocce M., 2018, MNRAS, 473, 3051
Jing Y. P., 2000, ApJ, 535, 30
Kacprzak T., Zuntz J., Rowe B., Bridle S., Refregier A., Amara A., Voigt L., Hirsch M., 2012, MNRAS, 427, 2711
Kilbinger M., 2015, Rep. Prog. Phys., 78, 086901
Kilbinger M. et al., 2013, MNRAS, 430, 2200
Kitching T. D. et al., 2014, MNRAS, 442, 1326
Kitching T. D., Taylor P. L., Capak P., Masters D., Hoekstra H., 2019, preprint (arXiv:1901.06495)
Knebe A. et al., 2011, MNRAS, 415, 2293
Köhlinger F. et al., 2017, MNRAS, 471, 4412
Komatsu E. et al., 2011, ApJS, 192, 18
Krause E., Eifler T., 2017, MNRAS, 470, 2100
Labatie A., Starck J. L., Lachièze-Rey M., 2012, ApJ, 760, 97
Lacey C., Cole S., 1993, MNRAS, 262, 627
Lange J. U., van den Bosch F. C., Zentner A. R., Wang K., Hearin A. P., Guo H., 2019, MNRAS, 490, 1870
Laureijs R. et al., 2011, preprint (arXiv:1110.3193)
Lee S. et al., 2019, MNRAS, 489, 2887
Lesgourgues J., Pastor S., 2006, Phys. Rep., 429, 307
LSST Science Collaboration, 2009, preprint (arXiv:0912.0201)
Madau P., Diemand J., Kuhlen M., 2008, ApJ, 679, 1260
Martinet N. et al., 2018, MNRAS, 474, 712
Marulli F. et al., 2013, A&A, 557, A17
Marulli F., Veropalumbo A., Moresco M., 2016, Astron. Comput., 14, 35
Massara E., Villaescusa-Navarro F., Viel M., 2014, J. Cosmol. Astropart. Phys., 2014, 053
Meneghetti M. et al., 2008, A&A, 482, 403
Meneghetti M. et al., 2014, ApJ, 797, 34
Merten J. et al., 2015, ApJ, 806, 4
Metcalf R. B., Petkova M., 2014, MNRAS, 445, 1942
Miller L. et al., 2013, MNRAS, 429, 2858
Monaco P., Theuns T., Taffoni G., 2002, MNRAS, 331, 587
Monaco P., Sefusatti E., Borgani S., Crocce M., Fosalba P., Sheth R. K., Theuns T., 2013, MNRAS, 433, 2389
Montero-Dorta A. D. et al., 2020, preprint (arXiv:2001.01739)
Munari E., Monaco P., Sefusatti E., Castorina E., Mohammad F. G., Anselmi S., Borgani S., 2017, MNRAS, 465, 4658
Navarro J. F., Frenk C. S., White S. D. M., 1996, ApJ, 462, 563 (NFW)
Neto A. F. et al., 2007, MNRAS, 381, 1450
Paranjape A., Sheth R. K., Desjacques V., 2013, MNRAS, 431, 1503
Peacock J. A., Dodds S. J., 1996, MNRAS, 280, L19
Peebles P. J. E., 1980, The Large-Scale Structure of the Universe. Princeton Univ. Press, Princeton, NJ
Peebles P. J. E., 1993, Principles of Physical Cosmology, Princeton Univ. Press, Princeton, NJ
Percival W. J. et al., 2014, MNRAS, 439, 2531
Petkova M., Metcalf R. B., Giocoli C., 2014, MNRAS, 445, 1954
Planck Collaboration I, 2014, A&A, 571, A1
Planck Collaboration XIII, 2016, A&A, 594, A13
Planck Collaboration XXIV, 2016, A&A, 594, A24
Postman M. et al., 2012, ApJS, 199, 25
Poulin V., Boddy K. K., Bird S., Kamionkowski M., 2018, Phys. Rev. D, 97, 123504
Prada F., Scóccola C. G., Chuang C.-H., Yepes G., Klypin A. A., Kitaura F.-S., Gottlöber S., Zhao C., 2016, MNRAS, 458, 613
Ragagnin A., Dolag K., Moscardini L., Biviano A., D'Onofrio M., 2019, MNRAS, 486, 4001
Refregier A. et al., 2004, AJ, 127, 3102
Roncarelli M., Moscardini L., Borgani S., Dolag K., 2007, MNRAS, 378, 1259
Sánchez A. G. et al., 2012, MNRAS, 425, 415
Sánchez A. G. et al., 2014, MNRAS, 440, 2692
Sato M., Nishimichi T., 2013, Phys. Rev. D, 87, 123538
Sawala T. et al., 2015, MNRAS, 448, 2941
Schneider A., Stoira N., Refregier A., Weiss A. J., Knabenhans M., Stadel J., Teyssier R., 2020, JCAP, 2020, 019
Scoccimarro R., Zaldarriaga M., Hui L., 1999, ApJ, 527, 1
Shan H. et al., 2018, MNRAS, 474, 1116
Sheth R. K., Jain B., 2003, MNRAS, 345, 529
Sheth R. K., Tormen G., 1999, MNRAS, 308, 119
Sheth R. K., Tormen G., 2004a, MNRAS, 349, 1464
Sheth R. K., Tormen G., 2004b, MNRAS, 350, 1385

Simon P., King L. J., Schneider P., 2004, A&A, 417, 873
Smith R. E. et al., 2003, MNRAS, 341, 1311
Somerville R. S., Davé R., 2015, ARA&A, 53, 51
Springel V., 2005, MNRAS, 364, 1105
Takada M., Jain B., 2004, MNRAS, 348, 897
Takahashi R., Sato M., Nishimichi T., Taruya A., Oguri M., 2012, ApJ, 761, 152
Tessore N., Winther H. A., Metcalf R. B., Ferreira P. G., Giocoli C., 2015, J. Cosmol. Astropart. Phys., 2015, 036
Tinker J., Kravtsov A. V., Klypin A., Abazajian K., Warren M., Yepes G., Gottlöber S., Holz D. E., 2008, ApJ, 688, 709
van den Bosch F. C., 2002, MNRAS, 331, 98
Watson W. A., Iliev I. T., D'Aloisio A., Knebe A., Shapiro P. R., Yepes G., 2013, MNRAS, 433, 1230
Wechsler R. H., Bullock J. S., Primack J. R., Kravtsov A. V., Dekel A., 2002, ApJ, 568, 52
Wetzel A. R., Hopkins P. F., Kim J.-h., Faucher-Giguère C.-A., Kereš D., Quataert E., 2016, ApJ, 827, L23
White S. D. M., Rees M. J., 1978, MNRAS, 183, 341
Wilkinson M. I., Kleyna J. T., Evans N. W., Gilmore G. F., Irwin M. J., Grebel E. K., 2004, ApJ, 611, L21
Wright A. H., Hildebrandt H., van den Busch J. L., Heymans C., Joachimi B., Kannawadi A., Kuijken K., 2020, preprint (arXiv:2005.04207)
Yao J., Pedersen E. M., Ishak M., Zhang P., Agashe A., Xu H., Shan H., 2020, MNRAS, 495, 3900
Zehavi I. et al., 2011, ApJ, 736, 59
Zehavi I., Kerby S. E., Contreras S., Jiménez E., Padilla N., Baugh C. M., 2019, ApJ, 887, 17
Zhao D. H., Mo H. J., Jing Y. P., Börner G., 2003a, MNRAS, 339, 12
Zhao D. H., Jing Y. P., Mo H. J., Börner G., 2003b, ApJ, 597, L9
Zhao D. H., Jing Y. P., Mo H. J., Bnörner G., 2009, ApJ, 707, 354

APPENDIX A: HALO COVARIANCE WEAK LENSING POWER SPECTRA

In Fig. A1, we display the covariance matrices of the convergence power spectra from 512 different maps build using only haloes, i.e. on large scale the convergence power spectra are not forced to follow linear theory. The three panels from left to right show the convergence power spectrum covariance at three different source redshifts: $z_s = 0.5$, 1.4, and 4.

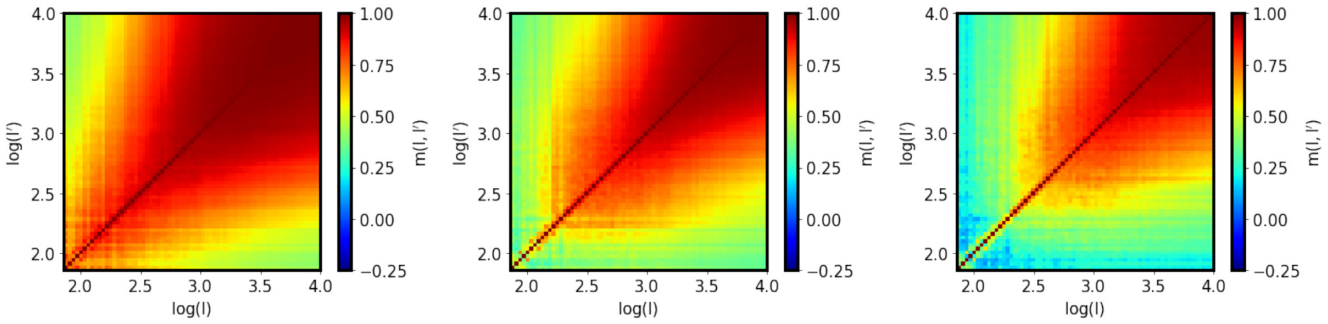

Figure A1. Same as Fig. 14 but considering in our convergence maps only the halo contributions: PINOCCHIO plus WL-MOKA (only haloes). The three panels display the covariance matrix for sources at $z_s = 0.5$, 1.4, and 4 from left to right, respectively.

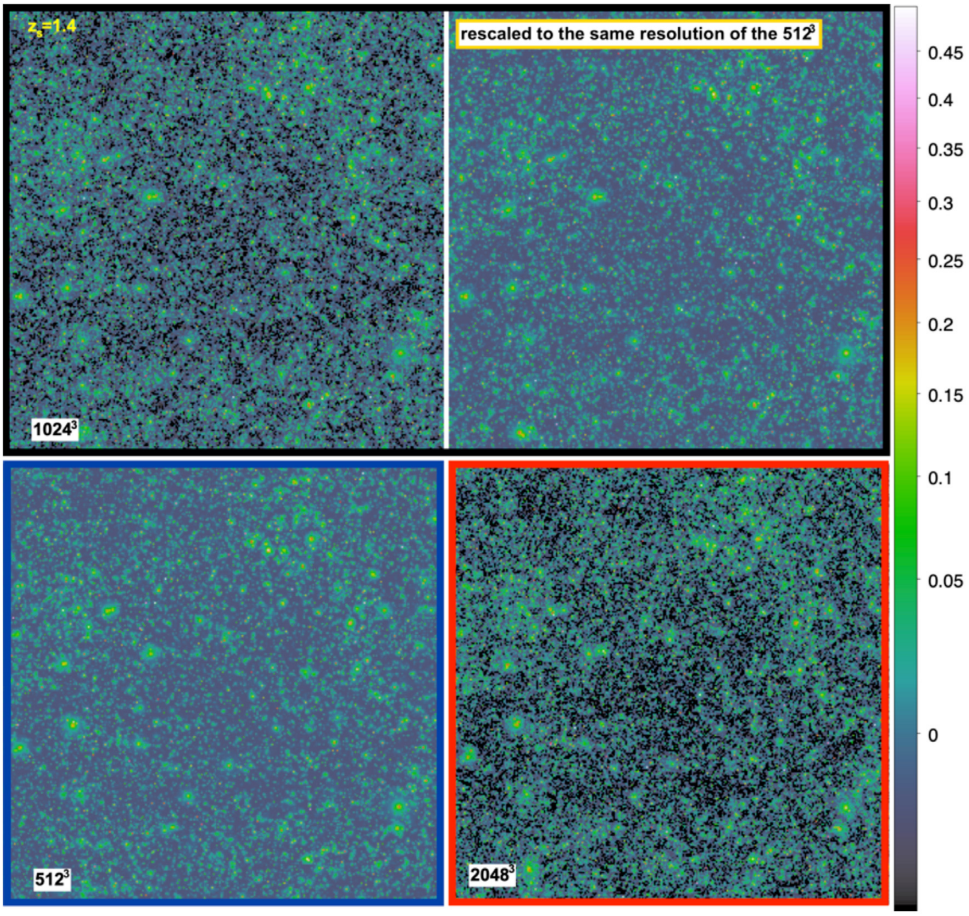

Figure B1. Convergence maps at $z_s = 1.4$ for the same randomization but for different runs. Top left, bottom left, and bottom right display the convergence maps for the PINOCCHIO runs with 1024^3, 512^3, and 2048^3 particles, top right shows the convergence map build with running WL-MOKA on the 1024^3 run but considering all haloes with mass larger than 5.6×10^{12} $M_\odot\, h^{-1}$, which corresponds to the halo mass resolution of the 512^3. In all cases we have adopted 3LPT displacement field and all maps are resolved with the same resolution of 2048 × 2048 pixels on an angular scale of 5 deg by side.

APPENDIX B: CONVERGENCE MAPS AT DIFFERENT GRID RESOLUTIONS

In this section, we display the convergence maps constructed adopting different particle and grid resolutions when running PINOCCHIO while using the same seed and phases when displacing particles and haloes (3LPT) from the ICs. Fig. B1 shows the convergence map for sources at $z_s = 1.4$; top left, bottom left, and bottom right panels exhibit the results when running WL-MOKA on the PLC halo catalogues of the 1024^3, 512^3, and 2048^3 PINOCCHIO simulations, respectively. In all cases, we notice, the LSS is similar but the haloes have different displacements. The top right panel shows the convergence map constructed on the halo catalogue of the 1024^3 run, but considering only systems more massive than 5.6×10^{12} $M_\odot\, h^{-1}$, which corresponds to the halo mass resolution of the 512^3. We recall for the reader that when building the convergence maps we assume the average to be zero (Hilbert et al. 2020) and that they are resolved with 2048 × 2048 pixels on an angular scale of 5 deg on a side.

In Fig. B2, we show the normalized probability distribution function per pixel in the maps presented in Fig. B1. The different colours refer to the various runs and the arrows indicate the standard deviations of the distributions.

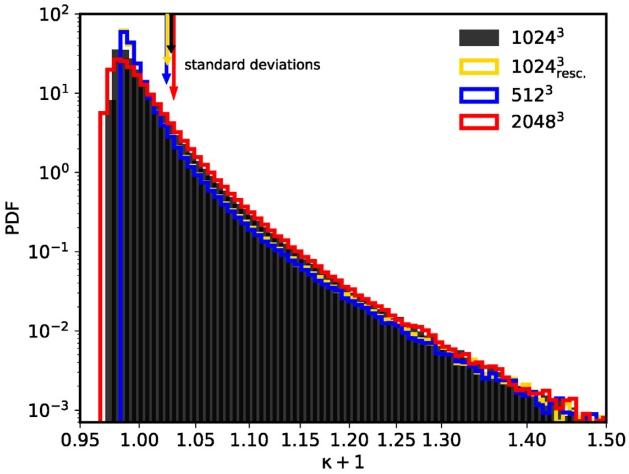

Figure B2. Probability distribution function per pixel of the convergence maps presented in Fig. B1. The arrows mark the standard deviation of the distributions, we recall the reader that by construction the maps have average equal to zero (Hilbert et al. 2020).

This paper has been typeset from a TEX/LATEX file prepared by the author.